Chemical Science

ROYAL SOCIETY OF CHEMISTRY

EDGE ARTICLE

View Article Online
View Journal | View Issue

Check for updates

Cite this: *Chem. Sci.*, 2025, **16**, 9766

All publication charges for this article have been paid for by the Royal Society of Chemistry

Synthesis of synergistic catalysts: integrating defects, SMSI, and plasmonic effects for enhanced photocatalytic CO_2 reduction†

Rajesh Belgamwar,‡[a] Charvi Singhvi, ‡[a] Gunjan Sharma, ‡[a] Vinod K. Paidi, [b] Pieter Glatzel, [b] Seiji Yamazoe, [c] Pradip Sarawade [d] and Vivek Polshettiwar *[a]

Received 14th February 2025
Accepted 25th April 2025

DOI: 10.1039/d5sc01166c

rsc.li/chemical-science

This study explores how the strategic material design introduced synergetic coupling of strong metal–support interaction (SMSI) between copper (Cu) nanoparticles and titanium dioxide (TiO_2) loaded on dendritic fibrous nanosilica (DFNS), defects within TiO_2, and localized surface plasmon resonance (LSPR) of Cu. Mechanistic insights were gained using *in situ* high-energy radiation fluorescence detection X-ray absorption near edge structure (HERFD-XANES) spectroscopy, electron microscopy, and finite-difference time-domain (FDTD) simulations. The introduction of copper nanoparticles onto the TiO_2 surface induces a change in the electronic structure and surface chemistry of TiO_2, due to the electronic interactions between Cu sites and TiO_2 at the interface, inducing SMSI. This resulted in enhancing light absorption, efficient charge transfer, reducing electron–hole recombination and enhancing the overall catalytic efficiency. The activation energy for CO_2 reduction was significantly reduced in light as compared to dark. Control experiments revealed a dominant role of photoexcited hot carriers, alongside photothermal effects, in driving CO_2 reduction, supported by super-linear light intensity dependence and reduced activation energies. The unique interplay of O-vacancy defects, electron–hole separation in TiO_2 and LSPR effects in Cu led to the excellent performance of the DFNS/TiO_2–Cu10 catalyst. The catalyst outperformed the reported photocatalytic systems with a CO production rate of ~3600 mmol g_{Cu}^{-1} h^{-1} (360 mmol g_{cat}^{-1} h^{-1}) with nearly 100% selectivity. A reaction mechanism was proposed based on the intermediates observed using the *in situ* diffuse reflectance infrared Fourier transform spectroscopy (DRIFTS) and co-related to the electron transfer pathways to different reactants using HERFD-XANES. The study concluded that the synergistic coupling of Cu LSPR, charge carrier separation *via* SMSI at the Cu–TiO_2 interface, and O-vacancy defects stabilized by SMSI enhance the photocatalytic CO_2 reduction performance of this hybrid system.

Introduction

The rising amounts of carbon dioxide (CO_2) in the Earth's atmosphere have become a major worldwide problem, necessitating the development of novel climate-change mitigation techniques. Among the several options, photocatalytic CO_2 reduction has emerged as a viable pathway for converting carbon dioxide into useful fuels, with carbon monoxide (CO) serving as a major step.[1–3] Many photocatalytic systems have been developed to resolve this issue, including the semiconductor and plasmon-based catalysts.[4–11] While photocatalytic CO_2 reduction to CO is a promising approach, it is essential to recognize that other reduction products, such as methane (CH_4) and methanol (CH_3OH), are also commonly produced in CO_2 reduction reactions. The selectivity of the process, whether it favors the formation of CO, CH_4, or CH_3OH, depends on various factors, including the catalyst, reaction conditions, and the reaction pathway. The development of catalysts with high selectivity for CO production remains a significant challenge, as the competition between different reduction pathways can reduce efficiency. Among semiconductors, titanium dioxide has been extensively used as a photocatalyst.[12–14] To tackle the problems of limited visible light response and high charge carrier recombination rate of these photocatalysts, different strategies were employed like defect creation,[15–17] use of metal nanoparticles (NPs) as cocatalysts, *etc.*[18–22] Yet their practical utility is still limited due to

---

[a] *Department of Chemical Sciences, Tata Institute of Fundamental Research, Mumbai, 40005, India. E-mail: vivekpol@tifr.res.in*

[b] *ID26, European Synchrotron Radiation Facility, Grenoble, France*

[c] *Department of Chemistry, Graduate School of Science, Tokyo Metropolitan University, Tokyo 192-0397, Japan*

[d] *National Centre for Nanoscience and Nanotechnology, Department of Physics, University of Mumbai, Mumbai 400098, India*

† Electronic supplementary information (ESI) available: Experimental details, Scheme S1, Fig. S1 to S15, and Table S1–S4 is available for this paper. See DOI: https://doi.org/10.1039/d5sc01166c

‡ Shared first authors.

limited efficiency and CO production rate. Thus, a novel approach to developing sustainable catalysts represents a fundamental pursuit in catalytic materials research.

In this study, we propose an innovative strategy that utilizes synergistic coupling of defects, strong metal–support interaction (SMSI) and localized surface plasmon resonance (LSPR). This study hypothesizes that manipulating plasmonic resonance, defects, and SMSI can provide a novel way of tuning the photocatalytic performance (production rate, selectivity and stability) of the catalyst.

LSPR exhibited by various metal nanoparticles allows the concentration of light energy and can pave new ways for chemical transformations with better activities and selectivities.[23–41] Defects have long been employed as a means to fine-tune the catalytic behaviour of materials,[42–48] yet their potential for precisely modulating photocatalytic behaviours of plasmonic catalysts remained relatively unexplored. Building upon our ongoing research into defect-tuned catalysis,[49–52] using dendritic fibrous nanosilica (DFNS)-based catalysts,[53,54] and plasmonic catalysis,[9,10,55–57] this work aims to develop hybrid plasmonic-defected photocatalysts for CO_2 to CO conversion. The hypothesis was that the activation energy could be significantly reduced in light owing to the synergistic interplay of SMSI-stabilized oxygen vacancies, and enhanced charge carrier separation.

Leveraging the electronic tuning of Ti conduction bands of TiO_2 upon incorporation of Cu atoms and defect creation, the electron transfers between the TiO_2 and Cu were enhanced.[58–60] Owing to this enhancement in charge transfer, the electron–hole pair recombination was inhibited due to spatial separation. The electron transfer between the semiconductor TiO_2 and plasmonic Cu under illumination was deduced by employing *in situ* high-energy radiation fluorescence detection X-ray absorption near edge structure (HERFD-XANES), which also helped in elucidating the charge transfer processes to the reactants.

Detailed spectroscopic analysis (HERFD-XANES, UV-Vis, IR), as well as finite-difference time-domain (FDTD) simulations, were performed to understand this synergy and the enhanced electron transfer rate between active site and reactants was understood, and a molecular reaction mechanism was deduced using *in situ* DRIFTS studies. The synergistic interplay of defect creation and efficient charge separation effect signifies this remarkable improvement in catalytic performance, which is discussed in the subsequent sections.

Results and discussions

Photocatalytic CO_2 reduction

The catalysts were synthesized by TiO_2 coating on each fibre of DFNS, followed by loading different amounts of Cu NPs (0.05 wt%, 4 wt%, 10 wt% and 20 wt%) (Table S1†), *via* deposition–precipitation of Cu salt directly on TiO_2 surface followed by calcination in air and thermal reduction in H_2 environment (refer ESI† for detailed protocol). The photocatalytic CO_2 reduction was carried out in a flow reactor, utilizing a xenon lamp as the light source (5.1 W cm^{-2}, 230–1100 nm) and a quartz window to facilitate the light irradiation (Scheme S1†). The catalyst powder was loaded in a porous alumina crucible of a flow reactor. Carbon dioxide and hydrogen were introduced at flow rates of 80 mL min^{-1} and 1 mL min^{-1}, respectively, with a total flow rate of 101 mL min^{-1}, balanced with argon. The products were monitored through online micro-gas chromatography (micro-GC). Under the influence of light, the catalytic reaction proceeded without the need for additional external heating.

Among the various Cu-loaded catalysts studied, the DFNS/TiO_2–Cu10 catalyst exhibited the highest activity, achieving nearly 100% selectivity for the production of CO (Fig. 1a). Subsequently, we optimized the total flow rate for the best DFNS/TiO_2–Cu10 catalyst under the light conditions (wavelength range of 230–1100 nm and intensity of 5.1 W cm^{-2}), operating at 1 bar pressure. The optimization process identified a total flow rate of 101 mL min^{-1} as the most effective flow, resulting in a CO productivity of 3601 mmol g_{Cu}^{-1} h^{-1} (360 mmol g_{cat}^{-1} h^{-1}) (Fig. 1b). Notably, increasing the flow rate beyond this optimal flow reduced catalytic activity due to the reduced residence time of reactant gases on the active sites, attributed to the high space velocity of the reactant gases. We further investigated the impact of different $CO_2 : H_2$ ratios while maintaining the total flow rate at 101 mL min^{-1}, balanced with argon. Argon was used as the inert gas to maintain the optimal gas hourly space velocity (GHSV) and thus the residence time of the reactant gases on the active sites. It was observed that the CO productivity was maximized at a $CO_2 : H_2$ ratio of 80 : 1 (Fig. 1c). It is worth noting that a very less $H_2 : CO_2$ ratio is required to achieve this high productivity along with high selectivity towards CO, which makes this system even more sustainable. Also, this finding suggests that the CO_2 activation is the challenging step of the process, therefore requiring a high concentration of CO_2 in the feed.

The long-term stability of DFNS/TiO_2–Cu10 for photocatalytic CO_2 reduction was assessed for ∼100 hours. Initially, there was a decrease in catalyst activity, with the CO production rate falling from 3601 to 1700 mmol g_{Cu}^{-1} h^{-1} during the first 30 hours of the reaction.

However, after this initial decline, the catalyst exhibited consistent stability throughout the entire 100 hour period (Fig. 1d). The initial loss could be due to some agglomeration of the Cu NPs which was observed in the STEM EDS mapping of the spent catalyst after 30 h (Fig. S1†). After this initial loss, the extended stability was attributed to the interaction established between the TiO_2 support and the active Cu sites within the catalyst. This allowed a controlled degree of agglomeration while ensuring a high dispersion of Cu nanoparticles (due to SMSI), a key factor contributing to this sustained stability. The high dispersion of stable Cu active sites on TiO_2 as a result of defect-tuned SMSI was confirmed by the high-angle annular dark-field scanning transmission electron microscopy (HAADF STEM) imaging and STEM EDS mapping of the spent catalyst (Fig. S1†).

The control experiments were carried out using only hydrogen or carbon dioxide and different catalyst components singularly. These experiments revealed no observable catalytic activity (Fig. 1e). Importantly, without Cu loading, DFNS/TiO_2

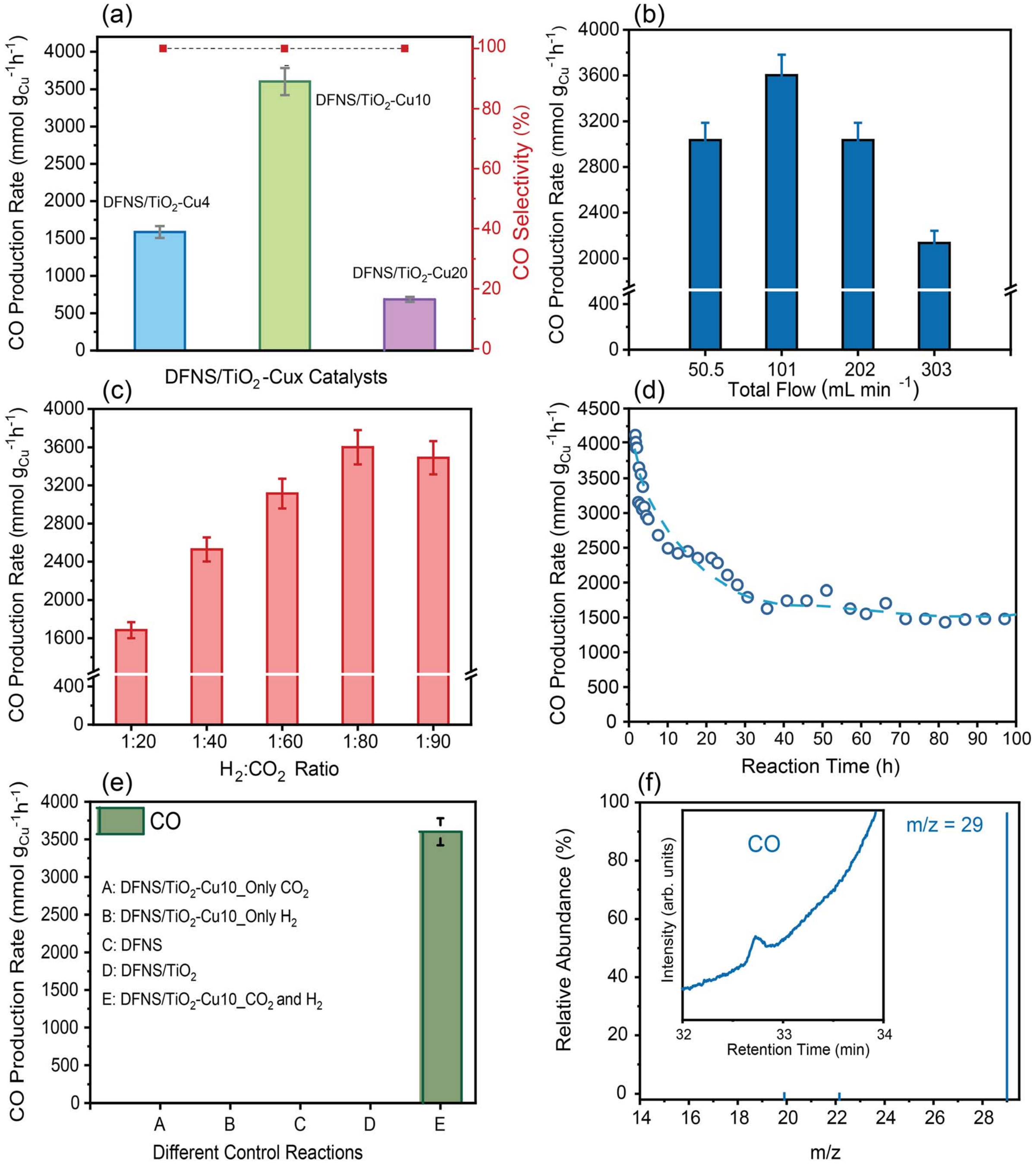

Fig. 1 Catalytic performance of DFNS/TiO$_2$–Cu for photocatalytic CO$_2$ reduction, (a) CO productivity using various Cu-loaded DFNS/TiO$_2$ catalysts (x denotes the Cu wt%) at 1 bar pressure, 80 : 1 CO$_2$: H$_2$ ratio with a total flow rate of 101 mL min^{-1}; Impact of (b) total flow (with 80 : 1 CO$_2$: H$_2$ ratio), (c) influence of CO$_2$: H$_2$ ratio (at 101 mL min^{-1} total flow) on CO production rate using DFNS/TiO$_2$–Cu10 catalyst; (d) long-term stability of DFNS/TiO$_2$–Cu10 catalyst; (e) control experiments using different catalysts under various reaction conditions; (f) mass spectra of ^{13}CO, when labelled ^{13}CO$_2$ was used as the feed gas (inset: gas chromatogram of CO).

showed no CO production. This underlines the crucial role of Cu in activating the DFNS/TiO$_2$ catalyst, reaffirming its significance in the CO$_2$ reduction process. To unequivocally confirm that the supplied CO$_2$ was the exclusive carbon source for CO production, we conducted an isotope experiment, replacing the standard ^{12}CO$_2$ feed gas with isotopically labelled ^{13}CO$_2$ gas. The resulting gas chromatography-mass spectrometry (GC-MS) analysis showed a distinctive signal corresponding to ^{13}CO ($m/z = 29$) in the mass spectrum (Fig. 1f). This analysis provided evidence that the product CO indeed originated from the ^{13}CO$_2$ feed gas.

Structural characterization of the DFNS/TiO$_2$–Cu10 catalyst

To understand the structure–activity relationship, it is of high importance to investigate the crystalline nature of the catalyst and further understand the catalytic performance and mechanism. The transmission electron microscopy (TEM) images of the fresh DFNS/TiO_2–Cu10 catalyst after H_2 treatment displayed uniform loading of Cu nanoparticles on the DFNS/TiO_2 sphere (Fig. 2a–f). Scanning transmission electron microscopy coupled with energy dispersive X-ray spectroscopy (STEM-EDS) elemental mapping indicated the high dispersion of Cu active sites on the TiO_2 support, with Cu and Ti signals appearing

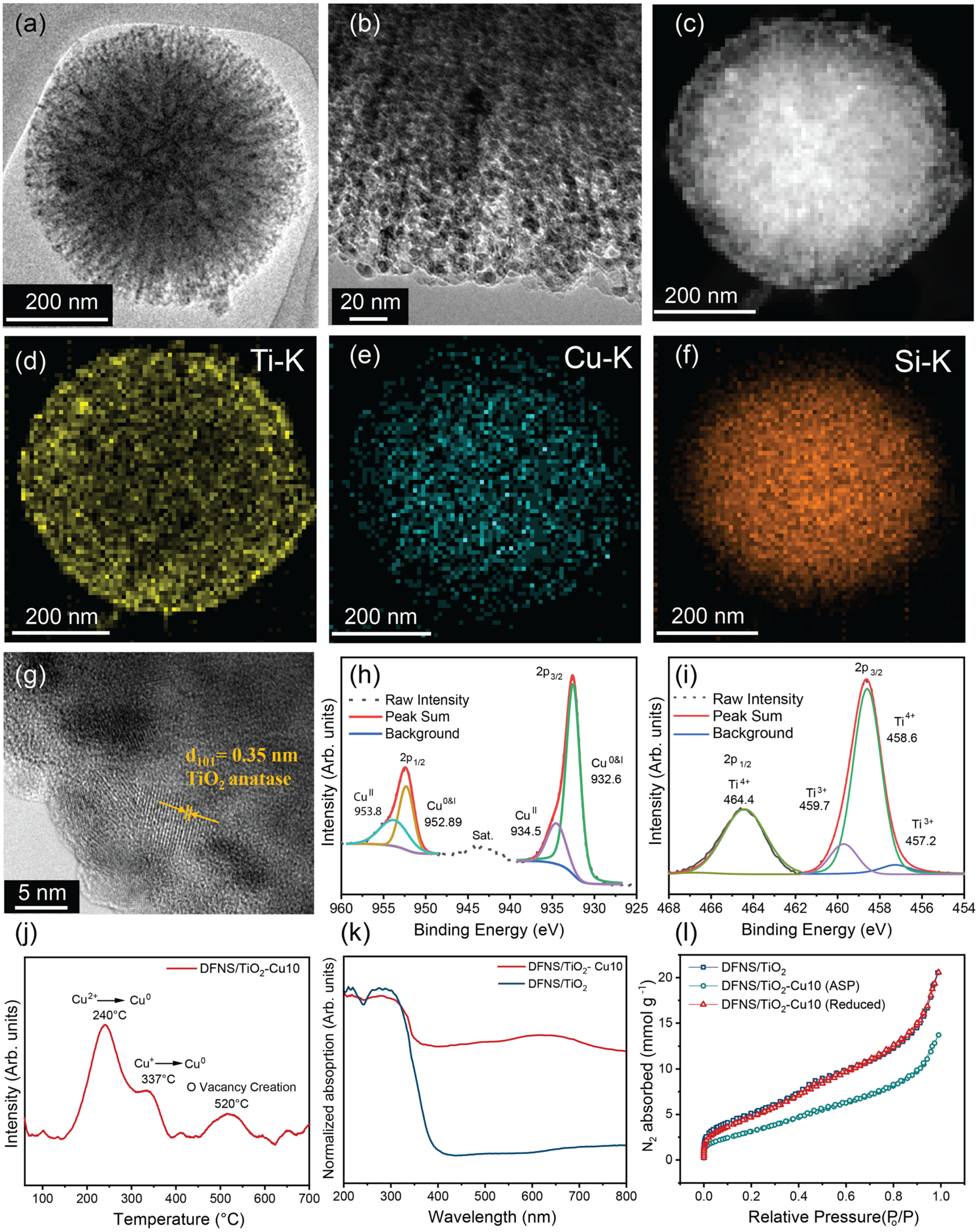

Fig. 2 DFNS/TiO_2–Cu10 catalyst characterisation, (a) and (b) HRTEM images; (c) HAADF-STEM images; (d)–(f) STEM-EDS elemental mapping; (g) HRTEM image showing anatase phase of TiO_2; XPS spectra for (h) Cu 2p and (i) Ti 2p; (j) TPR profile of DFNS/TiO_2–Cu10 as prepared (ASP) catalyst; (k) UV-Vis DRS (diffuse reflectance spectra) for DFNS/TiO_2 and DFNS/TiO_2–Cu10 (reduced) catalyst; (l) N_2 sorption isotherms for DFNS/TiO_2, DFNS/TiO_2–Cu10 (ASP) and reduced catalyst.

uniformly on the catalyst's surface (Fig. 2d–f). HAADF STEM images showed Cu NPs with varying particle size distribution with variable loading, with a mean particle size of 6.5 nm for DFNS/TiO_2–Cu10 (Fig. S2†). The high-resolution (HR) TEM images showed the lattice fringes of the anatase phase of TiO_2 (Fig. 2g) and (111) planes of Cu and Cu_2O (Fig. S3†).[61] Powder X-ray diffraction (PXRD) patterns of DFNS/TiO_2–Cu10 did not show patterns for anatase TiO_2 or Cu (Fig. S4†), which may be due to small crystallite size or the amorphous nature of the deposited sites.[51,52] X-ray photoelectron spectroscopy (XPS) indicated the presence of Cu^0 and Cu^+ species (Fig. 2h). Two sets of 2p peaks were seen in the Cu XPS 2p core level spectra; the first set included Cu $2p_{3/2}$ and Cu $2p_{1/2}$ peaks at 932.6 and 952.89 eV, respectively, which indicate the presence of copper with low valences, such as Cu^0 and Cu^+ (Fig. 2h).[62] The weak peaks of Cu $2p_{3/2}$ at 934.5 eV and Cu $2p_{1/2}$ at 953.8 eV in combination with the satellite peaks at 942 eV are typical characteristics of Cu^{2+}, which could occur due to oxidation during the XPS sample preparation.[62,63] In the high-resolution XPS spectrum of Cu-loaded DFNS/TiO_2, spin–orbit splitting results in the doublets, Ti $2p_{3/2}$ at binding energy 458.6 eV and Ti $2p_{1/2}$ at binding energy 464.4 eV (Fig. 2i). These peaks correspond to TiO_2 with Ti^{4+} sites.[63] Also, the shoulder at binding energy 459.7 eV corresponds to Ti^{3+} in TiO_2. The presence of Ti^{3+} state could be directly linked to the formation of oxygen vacancies, which was also confirmed by the temperature-programmed reduction (TPR) analysis of DFNS/TiO_2–Cu10 (Fig. 2j). It showed three distinct peaks corresponding to the reduction of Cu^{2+} to Cu^0, Cu^+ to Cu^0 and creation of oxygen vacancies. The resulting Cu^0 in contact with TiO_2 would interact with the oxygen from the network and form Cu^+–$[O_x]$–Ti^{3+}, which exhibited a reduction signal at ∼337 °C and finally, this oxygen was lost, creating vacancies at ∼520 °C.[64–66] These partially positive Cu sites are attributed to Cu undergoing SMSI with the TiO_2 support.

To probe the changes in the absorption profile of the catalyst after the incorporation of Cu, UV-Vis diffuse reflectance spectroscopy (DRS) data was recorded (Fig. 2k), which showed a broad band absorption profile for DFNS/TiO_2–Cu10, unlike DFNS/TiO_2 which showed a typical TiO_2 absorption profile lying entirely in the UV region. DFNS/TiO_2–Cu10 catalyst has highly dispersed Cu sites, which assisted in the formation of oxygen vacancies. The incorporation of defects as well as Cu helped to absorb a wide range of wavelengths by virtue of its LSPR effect.[67] The N_2 sorption isotherm analysis BET surface area calculations and the pore-size distribution analysis showed that the pores were occupied by loading the Cu salt on DFNS/TiO_2 and were then partially recovered by reduction due to the formation of highly dispersed Cu NPs (Fig. 2l, S5 and Table S2†).

In situ HERFD-XANES studies for insights into defects & SMSI

The variations in the Ti K-edge with reduction at various temperatures were investigated by measuring the Ti 1s core level HERFD-XANES spectra of TiO_2 (Fig. 3a–g and S6†). The spectral profiles conformed to the anatase phase of TiO_2 as also affirmed by HRTEM analysis (Fig. 2g).[68–70] The highest energy, most intense dipolar region of the spectrum (main edge ∼ 4.98 keV) primarily arises from the dipolar excitation of Ti 1s electrons to unoccupied Ti 4p states (Fig. S6†).[68] A decrease in energy and intensity of this edge, with increasing reduction temperature, was observed, resulting from poorer core hole screening and a reduced number of metal–ligand states (Ti 4p–O 2p hybrid orbitals in this system) available for 1s electron excitation.[68] The peak position energy difference is about 1.5 eV, compared to 0.9 eV between six- and five-coordinate Ti in glasses as reported by Farges *et al.*[68] This suggests an increase in five-coordinated Ti sites due to the formation of oxygen vacancies and the reduction of Ti^{4+} sites to Ti^{3+} with increasing temperatures.

In addition to the changes in the main-edge portion of the spectrum, significant variations in the energy and intensity of the Ti K-pre-edge peaks were observed, depending on the charge, bonding environment, and coordination number (CN).[69–72] As the CN decreases from 6, the loss of inversion symmetry allows the Ti 3d states to partially overlap with 4p states, introducing a dipolar component to the excitation and causing the peak intensity to increase. The reduction in the pre-edge energy with decreasing CN is likely due to alterations in final-state core-hole screening.[73–75] The splitting of the Ti 3d band of DFNS/TiO_2–Cu10 into t_{2g} and e_g states due to the crystal field effect is sensitive to the degree of hybridization and the number of ligand coordination.[75] This splitting results in four distinct peaks in the pre-edge region of Ti–K edge spectra, labelled A1–A4. The A1 peak is attributed to the quadrupolar 1s → 3d (t_{2g}) transition, while the A3 peak is attributed to the dipolar transition of 1s → 3d (t_{2g})–4p hybridized states, with a minor quadrupolar 1s → 3d (e_g) component. The A2 peak is linked to the quadrupole transitions of 1s to 3d (e_g)–4p hybridized states and A4 corresponds to the pure dipolar transitions of 1s → 3d (e_g)–4p hybridized states.[74–80] Although the peak assignments have been widely debated, it is generally accepted that A1 and A3 primarily probe the t_{2g} band, while A2 and A4 probe the e_g band. The absorption intensity of t_{2g} and e_g increases with rising catalyst reduction temperature, indicating the reconstruction of these bands through induced disorder/distortion in the structural matrix.[81–83] The separation of pre-edge peaks reflects the effect of the core–hole potential, which depends on the localization of the final states reached. Thus, A1 and A2 are associated with transitions to states strongly localized on the Ti atoms in the DFNS/TiO_2–Cu10 system.

On the other hand, studies on nanosized TiO_2 have shown that A2 is particularly sensitive to crystallinity and nanoparticle size, with its intensity correlating to low-coordinated Ti sites on the surface.[68,84] The intensity ratio of the two peaks (A2/A3) exhibited a linear increase with the reduction temperature up to 550 °C. However, at 650 °C, there was a sudden and marked increase in the A2 peak intensity. This abrupt change can be correlated to the enhanced oxygen vacancy formation at a higher reduction temperature. Such an increase in oxygen vacancies indicates significant lattice distortion within the TiO_6 octahedra, leading to a decrease in the coordination number of Ti sites. These findings are consistent with the spectral analysis conducted by Yogi *et al.*[74] At the surface, a five-coordinated

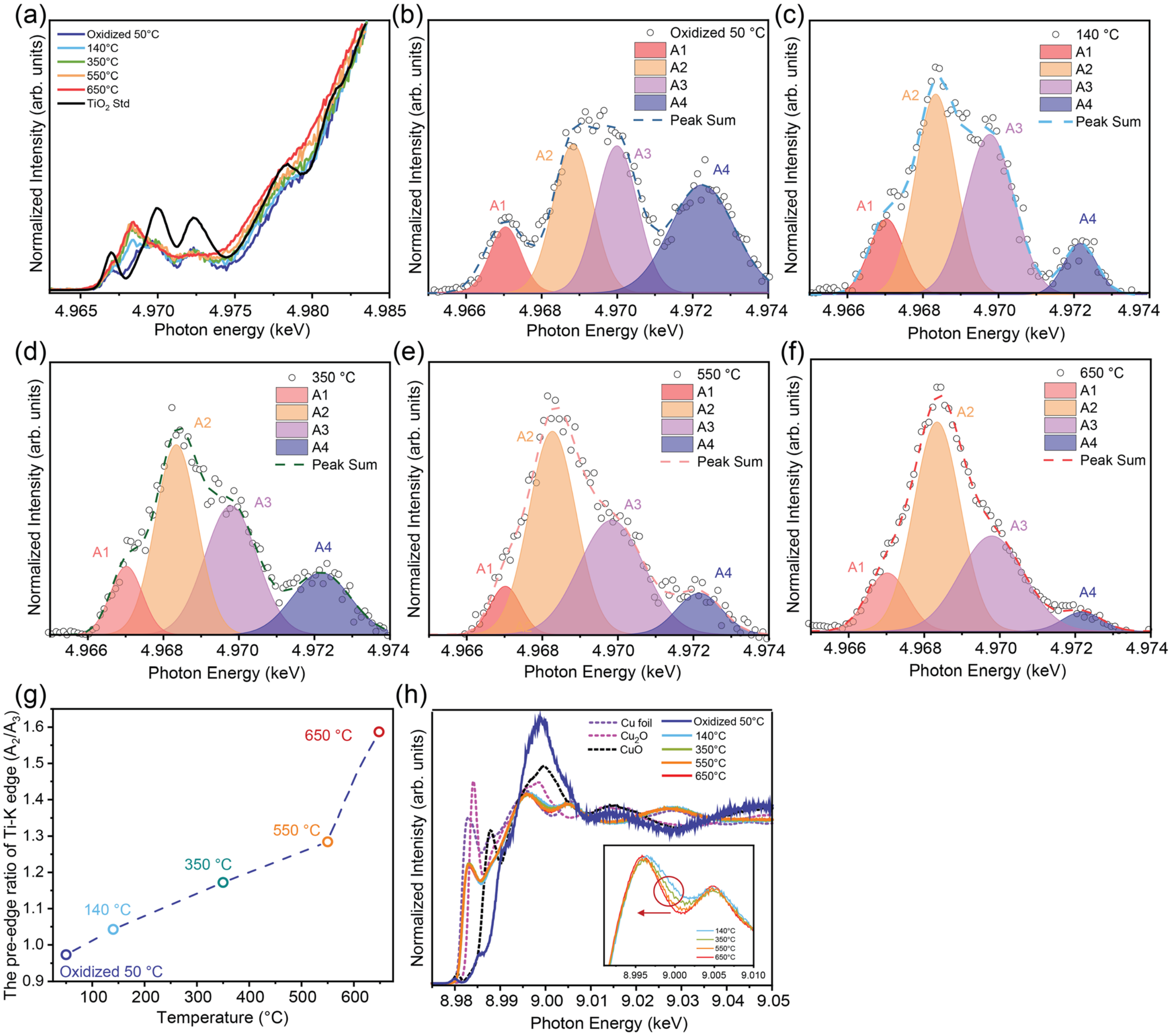

Fig. 3 *In situ* electronic and structural characterization of the catalyst. *In situ* HERFD-XANES of oxidized DFNS/TiO_2–Cu10 catalyst during *in situ* H_2 reduction conditions with 20 mL min^{-1} H_2 flow at various temperatures with a ramp of 8.5 °C min^{-1}, (a) Ti K-edge pre-edge region spectra; Gaussian curve fittings of anatase TiO_2 in the pre-peak region at different temperatures (b) 50 °C, (c) 140 °C, (d) 350 °C, (e) 550 °C, and (f) 650 °C; (g) A2/A3 ratio from the pre-edge of Ti K-edge *versus* temperature plot, (h) Cu-K edge XANES spectra.

geometry predominates, accounting for the observed distorted environments. This correlation suggests that the formation of oxygen vacancies plays a critical role in altering the local coordination and structural arrangement of Ti sites within the lattice.

A series of Cu K-edge XANES spectra recorded under *in situ* conditions (Fig. 3h) consisted of three major features labelled as A–C. The pre-edge feature at 8.980 keV (feature A) arises from transitions to spatially localized 3d states.[85–87] The shape of this pre-edge is influenced by the number of d-shell electrons, with its intensity proportional to the 3d–4p hybridization with its energy indicating the oxidation state. The presence of this feature, which is prominent in as-prepared catalysts, signifies Cu^{2+} since Cu and Cu^+ have filled 3d orbitals.[85] Upon exposure to a reducing environment, Cu^{2+} is readily reduced at 140 °C. Feature B, at 8.993 keV, corresponds to the 1s → 4s dipole transitions, with intensity directly proportional to the partial positive charge on Cu sites due to increased empty states in the 4s orbitals.[87–89] Feature C, the most intense white line at 8.996 keV, is attributed to 1s → 4p dipole transitions.[85,86] As the catalyst reduction temperature increases, the spectra shift to lower energies, indicating the reduction of Cu^{2+} and Cu^+ to metallic Cu. Even at 650 °C, the XANES pre-edge positions lie between those of Cu foil and Cu_2O, suggesting an oxidation state between 0 and +1.[89] This further supported the conclusions from H_2-TPR analysis that Cu sites in contact with TiO_2 exist in the Cu^+ state. *In situ* XANES analysis elucidated the interaction dynamics between TiO_2, its defects and the Cu NPs within the DFNS/TiO_2–Cu10 catalyst, revealing significant oxidation states and electron density distribution shifts among the Cu sites and TiO_2. It indicated the creation of oxygen vacancies or reduced Ti^{3+} species in TiO_2, which are associated with enhanced catalytic activity due to improved charge carrier dynamics. This reduction was accompanied by the oxidation of Cu sites at the interface from Cu^0 to Cu^+. This change is crucial for stabilizing the reduced Ti^{3+} sites and oxygen vacancies formed as well as for catalytic processes as it impacts the activation and transformation of reactants. These interactions between Cu and TiO_2 thereby alter the electronic states and band gap which result in enhanced photocatalytic performance because of better electron transfer rates, which is discussed in later sections. These investigations emphasise the crucial role of electronic structure adjustments, facilitated through SMSI, in optimising the catalyst's performance.

Comparison with best-reported photocatalytic systems

In the quest for superior photocatalytic systems for the conversion of CO_2 to CO, DFNS/TiO_2–Cu10, owing to the SMSI and plasmonic effects discussed above, the catalyst can surpass other photocatalysts in terms of CO productivity and selectivity. Thus the catalyst was evaluated against some of the most prominent photocatalysts that have been reported for photocatalytic CO_2 reduction.[10,12,64,90–121] Notably, DFNS/TiO_2–Cu10 exhibited good performance in terms of both CO production rate and CO selectivity (Fig. 4 and Table S3†). This indicates that our catalyst achieved the highest CO production rate, surpassing previously reported values, although this comparison is not perfect due to variations in reactor setup, reaction conditions and light intensities used by various reports. We chose to normalize the activity based on the active metal sites, as DFNS was used solely as a support to maximize metal dispersion. This approach did not apply to previously reported catalysts, such as Ni_3N and In_2O_{3-x}, as they lacked a support structure. The synergistic interplay of defect creation, plasmonic effects and efficient charge separation due to tuning of its band structure signifies this remarkable improvement in catalytic performance, which is discussed in the subsequent sections.

Insights into inhibitions of electron–hole recombination by coupling of defects & SMSI

The intricate mechanisms governing this photocatalytic CO_2 reduction process using DFNS/TiO_2–Cu10 were then studied. We explored the dependency of CO production rates on varying light intensities (Fig. 5a) while monitoring the catalyst bed temperature by inserting a thin thermocouple directly onto the

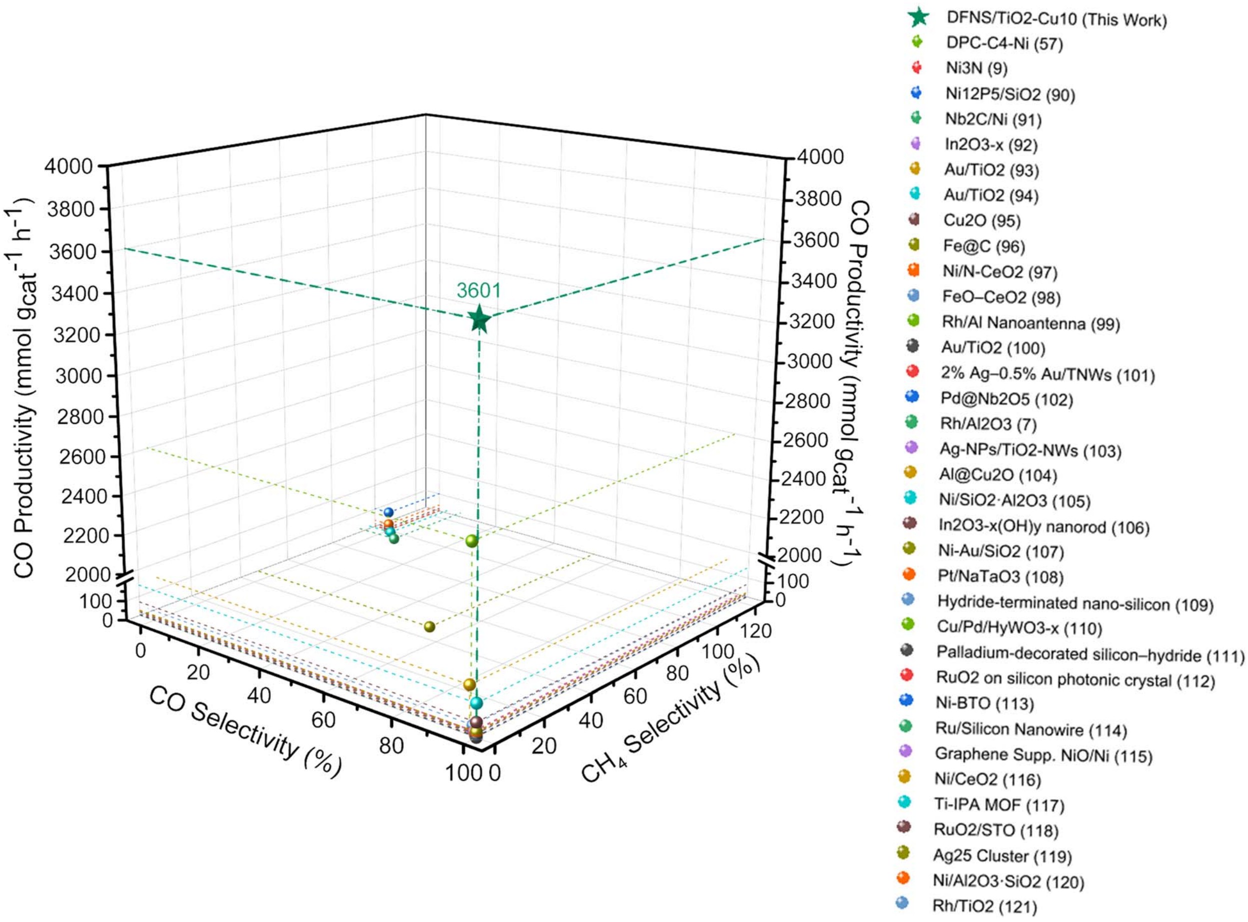

Fig. 4 Comparison of photocatalytic CO_2 reduction activity of DFNS/TiO_2–Cu10 catalyst with previously reported catalysts.

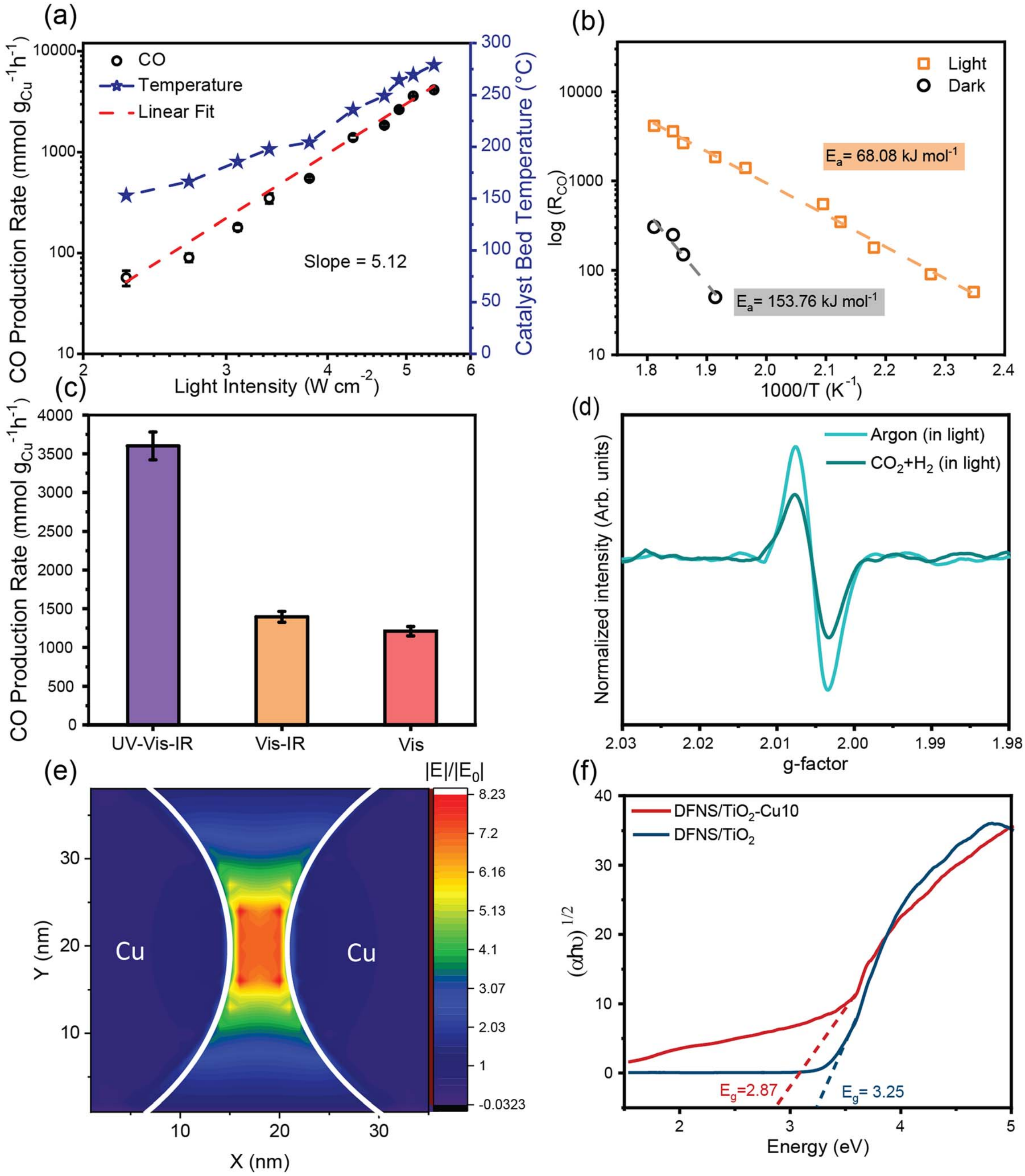

Fig. 5 Exploring the synergistic effects of defects, SMSI, and LSPR. (a) Relationship between CO production rate and varying light intensities (with corresponding catalyst bed temperature); (b) Arrhenius plots for activation energy calculation in light and dark for CO_2 reduction on DFNS/TiO_2–Cu10; (c) variation in CO production rate using different spectral regions of the Xe light source under constant light intensity of 3 W cm^{-2}; (d) EPR signal for oxygen vacancy in DFNS/TiO_2–Cu10 under inert (argon) and reaction (CO_2 + H_2) conditions (e) electric field enhancement in DFNS/TiO_2–Cu10 at 582 nm (source E_0 = 6197.8 V m^{-1}) (5.1 W cm^{-2}) using FDTD simulations; (f) optical band gap determination from UV-Vis DRS spectra.

catalyst bed, as outlined in Scheme S1.† Photocatalytic CO_2 reduction experiments were conducted at various light intensities (without external heating) and also in the dark (with external heating) (Fig. 5a and S6†). Under the light illumination intensity of 5.1 W cm^{-2}, an excellent CO production rate of 3601 mmol g_{Cu}^{-1} h^{-1} was achieved, accompanied by nearly 100% CO selectivity. Moreover, the super linearity of the light intensity dependence of CO production rate, characterized by the power law exponent of ~5.1 (Fig. 5a) is a signature of the hot-carrier multielectron mediated catalysis over plasmonic Cu (Fig. 5a).[122] A range of catalyst bed temperatures was attained at various light intensities without any external heating (Fig. 5a). To understand the contribution of photothermal effects, CO_2 reduction reactions were also carried out in the dark at these catalyst bed temperatures using external heating (Fig. S7†). Even at the highest temperature, only ~10% CO productivity compared to light was observed. This further highlights the significance of light in enhancing the CO_2 reduction rate.

To get better insight into the mechanism, activation energy was calculated from the Arrhenius plots plotted for light and dark conditions. The activation energy in light was found to be less than half of that required in dark (Fig. 5b). To understand the effect of plasmonic activation in detail, catalytic activity was evaluated at various wavelengths spanning the visible region and the CO production rate was found to be closely following the extinction profile of DFNS/TiO_2–Cu10 catalyst (Fig. S8a†). Wavelength-dependent apparent quantum efficiency (AQE) also corroborated with the extinction profile confirming the plasmonic activation-induced catalysis (Fig. S8b,† ESI note 1). To understand if the excited charge carriers formed in TiO_2 were also contributing to the chemical reaction, the impact of illumination in different regions of the light spectra on the catalytic performance was investigated (Fig. 5c). It was observed that when reaction was initiated under UV-Vis-IR light irradiation, a substantial increase in the CO productivity was witnessed as compared to visible light illumination with same intensity (Fig. 5c). The IR region had a less prominent effect on the catalyst activity as depicted by a lesser difference in the CO production rates obtained in Vis and Vis-IR illumination. An increase in UV-Vis-IR illumination depicted that the TiO_2 charge carriers were also actively contributing to the reaction after the incorporation of Cu (Fig. 5c) which was not observed in DFNS/TiO_2 under the same illumination (Fig. 1e). This was due to enhanced charge carrier separation by the formation of SMSI at Cu NP and TiO_2 interface that facilitated the charge transfers.[22,123] As TiO_2 excitons, plasmonic resonance and enhanced charge carrier separation played their role in enhancing the catalytic activity, attempts were then made to understand the role of oxygen vacancies during the CO_2 reduction reaction. Electron paramagnetic resonance (EPR) analysis of DFNS/TiO_2–Cu10 catalyst in argon flow showed a signal corresponding to the g factor of ~2.005 (Fig. 5d), which was attributed to the oxygen vacancies.[89,124] This signal intensity decreased as soon as the catalyst was exposed to reactant gases (CO_2 and H_2), which indicated the participation of oxygen vacancies during the reaction.

To visualize the local electric field enhancement due to LSPR of Cu, FDTD simulations were employed. The model consisted of a TiO_2 sheet over which Cu nanoparticles (5 nm) were deposited at a distance of 1.5 nm (Fig. 5e). The electric field was greatly enhanced (~8×) in the 'hot spot' formed between the Cu NPs, which could potentially polarise the reactant molecules.

To understand the dominance of TiO_2 interband and Cu LSPR in different regions of the UV-Vis spectrum in the catalyst, a wavelength-dependent FDTD simulation analysis was carried out, which showed the change in the direction of the electric field within the Cu NP in the range 380–400 nm (Fig. S9†). This change was consistent with the switching of the dominant light excitation behaviour from TiO_2 interband transitions to Cu LSPR in the visible region.[123] During the investigation of the changes in the band structure of TiO_2 after the incorporation of Cu *via* Tauc plot analysis, we observed a decrease in the band gap to 3.12 eV from 3.40 eV. It was due to its interaction of Cu with the Ti 3d bands in the TiO_2 network altering its electronic structure by the formation of an SMSI (Fig. 5f).[123,125] This contributed to reducing the charge carrier recombination rate as evidenced by the photoluminescence (PL) spectra in which the depletion in the intensity with increasing Cu loading indicated a lesser rate of recombination (Fig. S10†).[22,123] Our HRTEM analyses confirmed that TiO_2 in DFNS-TiO_2/Cu exhibit the anatase phase, further corroborated by HERFD-XAS of the Ti K pre-edge/edge. Furthermore, in this concentration range our XAS analysis indicated an increase in five-coordinated Ti and oxygen defect as well as a lattice distortion in the octahedra which is enhanced by SMSI effects after incorporating Cu.

In situ HERFD-XANES studies for insights into electron–hole dynamics

An *in situ* XAS measurement under UV-Vis illumination helped to probe the changes in electronic structure under light irradiation that can create electron–hole pairs and structural modulation. The *in situ* XAS Ti K-edge and Cu K-edge for DFNS/TiO_2–Cu10 were performed (Fig. 6a and b) and the difference in absorption intensity (ΔA) was plotted (Fig. 6d–i). An increase in the intensity of the Ti K-edge peak for the DFNS/TiO_2–Cu10 samples with a maximum at ~4965.5 eV was observed under UV-visible-light illumination (Fig. 6d). It indicates that the incorporation of Cu nanoparticles in TiO_2 altered the electronic structure of the catalyst.[68,84] Furthermore, this increase in the absorption intensity of DFNS-TiO_2/Cu-10 could be due to the LSPR effect of Cu NPs. It is well known that bare TiO_2 absorbs only in the UV range (Fig. 2k). The irradiation of DFNS/TiO_2–Cu10 sample with UV-visible light provided sufficient energy to generate excited electrons that flowed from the Ti 3d band of TiO_2 through the Schottky barrier junction (~0.6 eV between Cu and TiO_2) to the d orbital of the Cu NPs.[83,84] This charge transfer was further confirmed by Cu K-edge XANES spectra of the DFNS/TiO_2–Cu10 (Fig. 6g). The increase in ΔA for DFNS/TiO_2–Cu10 implies a significant decrease in the population of Ti 3d orbital under UV-Vis illumination. Because the band gap of TiO_2 lies in the UV region, the electrons present in the valence band get promoted to the Ti 3d band (conduction band) by UV light.[123–125] Further investigations of the electronic properties of Cu sites in light and dark were carried out using the XANES absorption profile for the Cu–K edge. An *in situ* XAS measurement under visible (420 nm) and UV (360 nm) illumination was carried out to observe the changes in the electronic structure under ultraviolet and visible irradiation that can create electron–hole pairs in TiO_2 and Cu, respectively. To understand the electronic properties of the Cu–TiO_2 interface, Cu K-edge XANES and extended X-ray absorption fine structure (EXAFS) spectra were recorded for DFNS/TiO_2–Cu20 and DFNS/TiO_2–Cu0.05 catalysts (Fig. S11–S14†). The sample with a lower concentration (~0.05% Cu) is expected to have more Cu–TiO_2 interfaces due to the smaller size of Cu nanoparticles formed and lower Cu–Cu coordination number (Fig. S13 and Table S4†), hence a better system to understand the electronic properties of

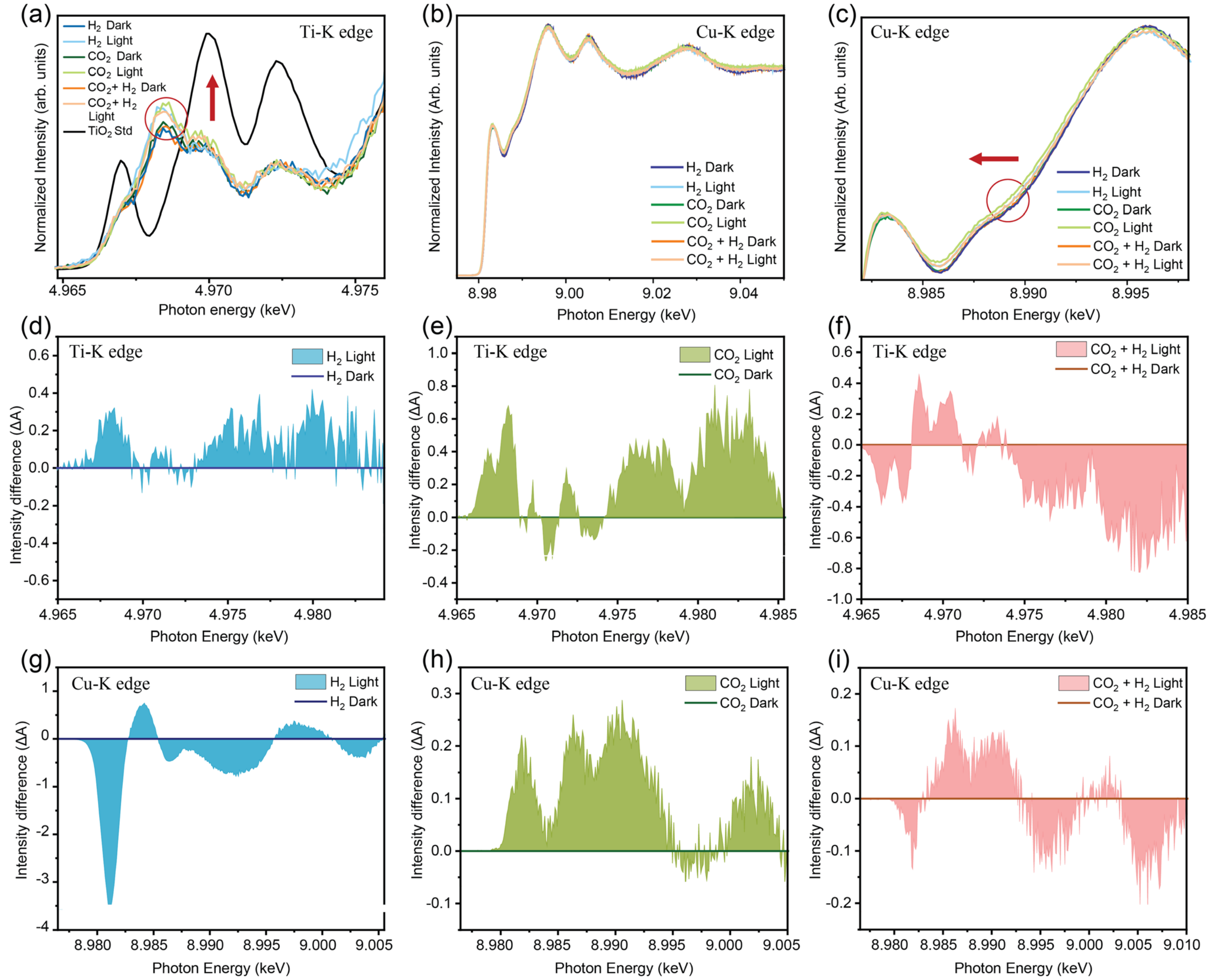

Fig. 6 *In situ* HERFD-XANES of reduced DFNS/TiO_2–Cu10 catalyst during *in situ* conditions under visible light illumination and dark conditions. (a) Ti–K pre-edge region, (b) and (c) Cu–K edge, pre-edge region; difference in absorption intensity (Δ*A*) between samples under irradiation and dark from panels a and b of (d)–(f) Ti–K edge during (d) H_2 flow, (e) CO_2 flow, (f) CO_2 + H_2 flow and Cu–K edge during (g) H_2 flow, (h) CO_2 flow, (i) CO_2 + H_2 flow (d) with 10 mL min^{-1} H_2 and 10 mL min^{-1} CO_2 flow (Δ*A* it was obtained after subtracting the intensity obtained during UV-visible illumination of the catalyst under different gaseous atmospheres with the corresponding absorption intensity in the dark in a similar atmosphere).

Cu sites directly in contact with TiO_2. As evident from feature A (Fig. S12a†), the pre-edge energy of Cu atoms in DFNS/TiO_2Cu-0.05 is shifted towards higher energy compared to DFNS/TiO_2Cu-20 indicating the latter possesses more Cu^+ character.[87]

The extent of SMSI and charge transfer efficiency in the DFNS/TiO_2–Cu catalysts is strongly influenced by Cu particle size, which varies with Cu loading. Smaller Cu nanoparticles offer a higher fraction of interfacial atoms in contact with TiO_2, strengthening SMSI and facilitating efficient electron transfer. The defect concentration also depended upon the Cu size and dispersion (Fig. S12b and c†), however, DFNS/TiO_2–Cu10 displayed the best balance between interfacial Cu atoms and exposed surface atoms, maximizing both SMSI and charge transfer as indicated by the suppressed PL intensity, and thus, catalytic activity. Higher loadings lead to agglomeration and reduced interfacial contact, lowering performance. When the catalyst DFNS/TiO_2Cu-0.05 was irradiated with light of wavelengths belonging specifically to UV (360 nm) and visible regions (420 nm), the Cu–K pre-edge was shifted to higher energy when compared to the dark (Fig. S11†) owing to the plasmonic excitation and related excitation of electrons to higher levels as a consequence of LSPR damping.[124] However, the shift in the pre-edge was less when the catalyst was irradiated with a 360 nm laser, where some interband transitions of TiO_2 are possible along with plasmonic excitations in Cu in comparison to 420 nm where absorption is dominated by Cu LSPR. This may be attributed to the transfer of excited state electrons from TiO_2 to the copper conduction band, as indicated by PL studies as well, following inter-band transitions upon 360 nm irradiation. This causes a slight increase in electron density on Cu in comparison to the pure plasmonic state at 420 nm where there is no electron density transfer from TiO_2.

The Ti–K edge spectra provided additional proof of this electron transfer from TiO_2 to Cu upon irradiation with light. The main-edge feature of the Ti–K edge XANES spectra (Fig. S14†) arises due to the transition between 1s orbitals to the hybridized Ti 4p states with the bonding states of nearest and next-nearest neighbouring atoms.[125–128] An increase in the intensity of this feature was observed in the Ti K-edge under UV-light (360 nm) illumination for the DFNS/TiO_2Cu-0.05 sample, indicating an increase in Ti unoccupied states. This result implied an excited electron charge transfer from Ti states to Cu empty states through the SMSI at the interface when the samples were illuminated by UV light (360 nm). This charge transfer would alter the band structure at the Cu nanoparticle–TiO_2 interface, resulting in the charge separation of photogenerated electron–hole pairs. Following this, the difference in absorption intensity (ΔA) obtained during UV-visible illumination of the catalyst was determined in an oxidizing atmosphere (CO_2). There was an increase in the overall intensity upon illumination with light in both the Ti K-edge and Cu K-edge. This means that the interactions with CO_2 under dark conditions were weak. The electron transfers from both TiO_2 and Cu active sites increased as the catalyst was impinged with light, implying that the activation of the CO_2 molecule was enhanced upon light illumination.

When the catalyst was provided with a redox atmosphere ($CO_2 + H_2$) in the presence of light, the CO_2 reduction to CO was feasible. The CO_2 molecule is activated when the O of CO_2 occupies the oxygen vacancy. Following this in the presence of H_2, the CO_2 molecule dissociates *via* a redox mechanism and leaves behind a weakly bonded oxygen in TiO_2 lattice. The hole of the electron–hole pairs generated in Cu due to LSPR was quenched by the H_2 and the labile oxygen to form H_2O, leaving behind high-energy hot electrons. These electrons are transferred into 3d bands of TiO_2, which are now effectively transferring them to the CO_2 molecule. Thus, increasing the electron density of TiO_2, which was also observed in the ΔA plots in the presence of $CO_2 + H_2$ as the oxygen vacancies were regenerated and H_2O was formed. The A2 peak indicates the presence of Ti^{3+} species and confirms that SMSI-stabilized oxygen vacancies persist during the reaction (Fig. 6a). Although oxygen vacancies are occupied by oxygen atoms from CO_2, they are simultaneously regenerated by the dissociation of H_2. Thus, the *in situ* detection of Ti^{3+} supports the dynamic nature and stability of these oxygen vacancies under catalytic conditions. On the other hand, not much change was observed in the overall electron density of Cu sites, as both electrons and hole were taken care of *via* different pathways. It was concluded from these studies that various phenomena can occur in DFNS/TiO_2–Cu system upon illumination with UV and visible light, like interband transitions from valence band of TiO_2 to conduction band upon irradiating it with UV light, the consequent charge carrier separation by transfer of excited electron density to Cu states and hot electron generation from the 4s-band of Cu (intraband excitation) and from the 3d-band of Cu (interband transition).[128–130] These investigations strongly indicate a synergistic coupling of Cu LSPR, charge carrier separation by an SMSI at the interface of Cu–TiO_2 and O-vacancy stabilized by Cu–TiO_2 SMSI in this hybrid DFNS/TiO_2–Cu system, which was responsible for its superior performance for photocatalytic CO_2 reduction.

Molecular mechanism of CO_2 to CO reduction by *in situ* DRIFTS

CO_2 reduction mechanisms generally follow two pathways: the redox mechanism and the dissociative mechanism.[131] To understand the mechanism of CO_2 reduction, an *in situ* diffuse reflectance infrared Fourier transform spectroscopy (DRIFTS) study was carried out using DFNS/TiO_2–Cu10 in light and dark conditions (Fig. 7).

No signal corresponding to CO was observed when only CO_2 was introduced in the reaction chamber (Fig. S15†). In the CO_2 + H_2 conditions, bands observed at 2934 cm^{-1} and 2854 cm^{-1} were attributed to the combination band (C–H) + ν_s (OCO) and ν (C–H) of bidentate formate species, respectively (Fig. 7b).[132,133] The broad signals from 2200–2000 cm^{-1} were assigned to gaseous CO.[134] The signal at ~1914 cm^{-1} corresponded to the C–O stretch of CO_2 adsorbed on oxygen vacancies in DFNS/TiO_2–Cu.[135] Additional band at 1776 cm^{-1} was attributed to the vibrational stretching mode of the OCO group of bicarbonate species[136] while the band 1585 cm^{-1} arose due to the formate species (Fig. 7c).[132,133] Based on these intermediates, we propose a reaction mechanism for CO_2 reduction over DFNS/TiO_2–Cu10 catalyst; (i) it involves the adsorption of CO_2 utilizing the O-vacancies causing the electron density to shift from Ti as observed in XANES, and plasmon-assisted H_2 dissociation over Cu NPs surface which led to increase in electron density on Cu as compared to only CO_2, suggested by XANES, (ii) the second step involves the formation of bicarbonate after the attack by terminal hydroxyl of the TiO_2 support, (iii) in the third step, one of the dissociated hydrogens attack the bicarbonate species resulting in the formation of formate which consequently leads to the loss of CO and H_2O resulting in the regeneration of oxygen vacancies (steps iv–vi).

Disentangling thermal and non-thermal pathways

Upon decay, plasmonic excitations generate non-equilibrium hot carriers (electrons and holes) on femtosecond timescales, followed by localized lattice heating *via* electron–phonon coupling on the order of picoseconds. These distinct energy dissipation pathways can activate surface-bound molecules *via* fundamentally different mechanisms.[137–141] To delineate the contribution of photothermal *versus* non-thermal (hot carrier-mediated) effects in the observed photocatalytic performance, we conducted a series of control experiments under dark, thermally heated, and light-irradiated conditions. A key observation is the markedly higher CO production rate under light irradiation compared to that in the dark at equivalent catalyst bed temperatures (Fig. S7†). This suggests that the enhancement cannot be solely attributed to photothermal heating but implicates the direct involvement of photoexcited charge carriers in driving the reaction.

To further probe the role of hot carriers, we examined the dependence of CO production on incident light intensity (Fig. 5a). The reaction rate exhibits a super-linear relationship,

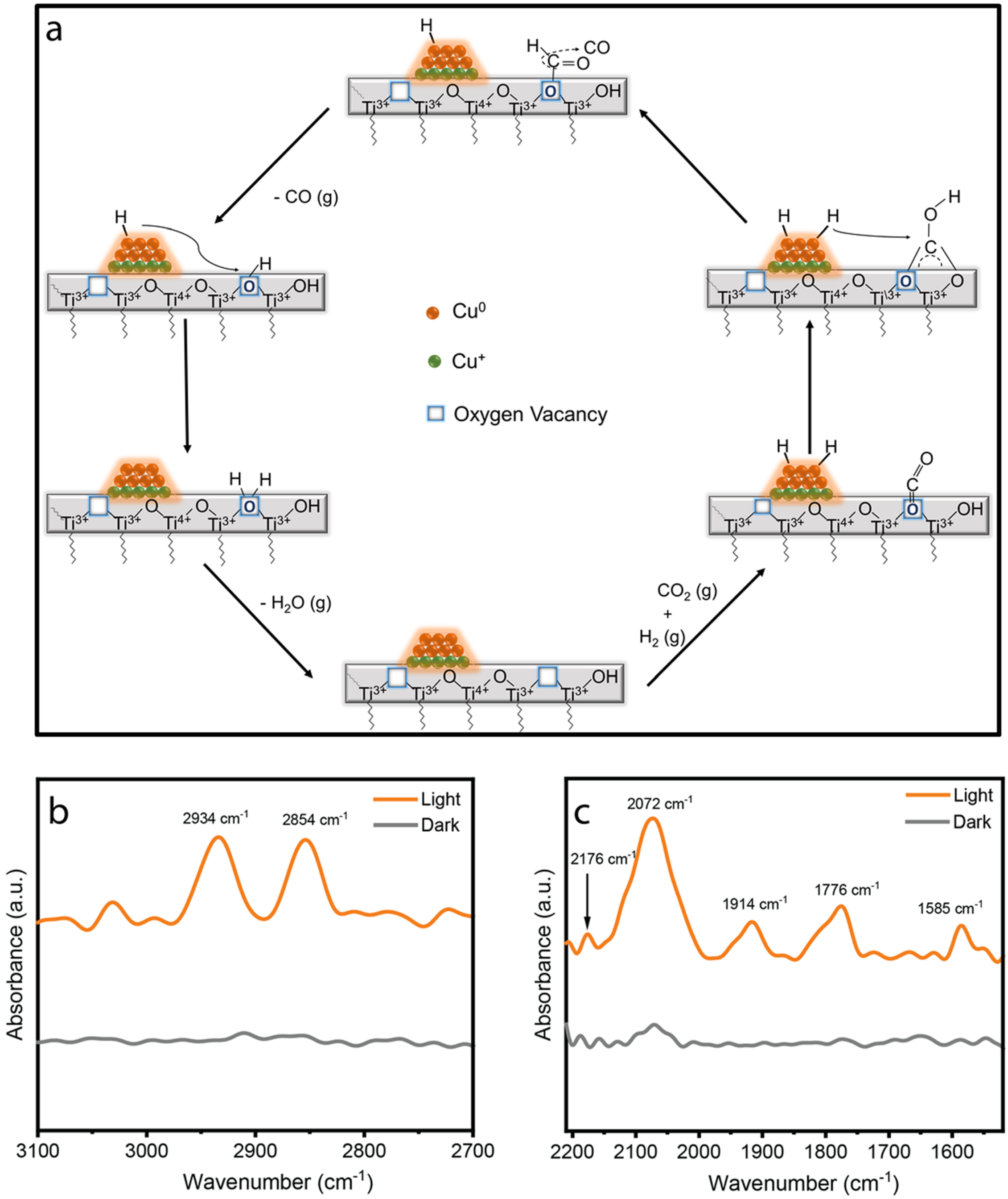

Fig. 7 Molecular mechanism of CO_2 reduction. (a) Proposed reaction mechanism for CO_2 reduction over DFNS/TiO_2–Cu10; (b) and (c) *in situ* DRIFTS spectra for DFNS/TiO_2–Cu10 under CO_2 + H_2 environment in light and dark conditions.

with a power-law exponent of $n \approx 5$. Such behaviour is emblematic of multi-electron-driven catalytic processes,[137] wherein a high flux of photoexcited electrons promotes sequential excitations prior to energy dissipation. This dynamic facilitates vibrational excitation and eventual bond cleavage, yielding an improved catalytic response that exceeds what is expected from photothermal effects alone. By contrast, purely photothermal processes display fundamentally different scaling behaviours. The temperature rise due to light absorption was approximately linear with incident light intensity (Fig. 5a). However, the corresponding reaction rate, governed by the Arrhenius equation, exhibits an exponential dependence on temperature. Therefore, unlike charge carrier-driven mechanisms, photothermal catalysis does not produce a super-linear dependence of reaction rate on light intensity.

Further support for a hot-carrier-mediated mechanism was derived from the comparison of apparent activation energies under dark and illuminated conditions (Fig. 5b). The substantial reduction in activation energy upon illumination indicates a mechanistic shift from classical thermally activated pathways to those facilitated by non-thermal charge carriers, affirming the dominant role of plasmonically generated hot electrons in catalysing the CO_2 reduction reaction.[137] Nevertheless, it is important to emphasize that while these experiments strongly support the involvement of hot carriers, photothermal effects are also contributing significantly to the overall activity. The two mechanisms, hot carrier-driven and photothermal, are inherently intertwined, operating concurrently under illumination.[137–141] Thus, a complete deconvolution of their individual contributions remains experimentally challenging, and both are likely to synergistically influence the catalytic performance under real reaction conditions.

Conclusions

The study reports a unique catalytic material synthesis protocol which integrates concepts of defects and plasmonics. It also demonstrates how the cooperative actions of SMSI between Cu and TiO_2, defects in TiO_2, and localized surface plasmon resonance collectively enhance the efficiency of the DFNS/TiO_2–Cu photocatalytic system in converting CO_2, using *in situ* HERFD-XANES spectroscopy.

In pursuit of a more sustainable and effective photocatalytic CO_2 reduction catalyst, in this work, we introduced a novel approach of material design that synergistically couples defects, SMSI at TiO_2–Cu interface, and localized surface plasmon resonance to enhance the photocatalytic performance of the catalyst. Our catalyst design involved coating TiO_2 on the fibres of DFNS, followed by generating varying-sized Cu NPs *via* heterogeneous nucleation on the TiO_2 surface. The DFNS/TiO_2–Cu10 catalyst, in particular, displayed a uniform distribution of Cu NPs on the DFNS/TiO_2 sphere, as confirmed by TEM, STEM-EDS, HAADF STEM imaging, XPS and *in situ* HERFD-XANES analysis. The TPR analysis of this catalyst revealed key features, including the reduction of Cu species and the creation of oxygen vacancies, which were essential for the establishment of SMSI and stabilizing the active sites. The DFNS/TiO_2–Cu10 catalyst exhibited exceptional activity (3601 mmol g_{Cu}^{-1} h^{-1}) and nearly 100% selectivity for CO production. The synergy of defect creation, efficient charge separation, and LSPR effect was pivotal in achieving these outcomes. In terms of long-term catalyst stability, although an initial decrease in activity was observed, attributed to Cu NP agglomeration, the catalyst maintained consistent performance over a 100 hour test period. This stability was credited to the inhibition of sintering and agglomeration due to strong electronic interactions between the defects in TiO_2 support and the active Cu sites through SMSI.

Our investigation into the synergistic coupling of defects, interface SMSI, and plasmonic effects by using EPR, PL and *in situ* XAS revealed intricate mechanisms of photocatalytic CO_2 reduction. The catalyst showed significantly higher CO productivity under light than in dark conditions, confirming the critical role of light in enhancing CO_2 reduction rates. FDTD simulations demonstrated an enhanced electric field concentrated in 'hot spots', aiding in reactant polarization. The inclusion of Cu also resulted in a reduced band gap, owing to the formation of SMSI with TiO_2. The molecular mechanistic understanding of CO_2 reduction was furthered by *in situ* DRIFTS studies. We proposed a multi-step reaction mechanism involving CO_2 adsorption, bicarbonate and formate formation, and product desorption, enhanced by the LSPR-induced concentrated electric field near Cu NPs. The mechanism elucidated by *in situ* XAS and DRIFTS underscores the pivotal role of oxygen vacancies and the LSPR generated hot electrons in enhancing the catalytic performance. This study demonstrated that the interplay between SMSI effects, plasmonic properties, and surface defects significantly enhances the catalytic performance for CO_2 reduction under both visible and UV-Vis irradiation. The integration of plasmonic materials with strong metal–support interactions and engineered defect sites can be extended to photocatalytic systems for water splitting, nitrogen reduction, and selective oxidation reactions. This strategy is a general platform for designing advanced catalysts for a wide range of energy and environmental applications.

Data availability

The data supporting this article have been included as part of the ESI.†

Author contributions

V. P. proposed the research direction, designed the project, and guided the project. V. P., R. B., C. S. and G. S. designed various experiments. R. B., C. S. and G. S. performed the experiments (synthesis, characterizations, catalysis, mechanism). V. P., C. S., P. G., V. K. P., and S. M. performed XAS studies. Data were analyzed by R. B., C. S., G. S., P. S., and V. P. The overall manuscript was written by V. P., R. B., C. S., G. S. Everyone commented on the manuscript.

Conflicts of interest

The authors declare no competing interests.

Acknowledgements

We acknowledge the funding support of the Department of Atomic Energy 12 R&D-TFR-RTI4003. We acknowledge the EM and XRD facility of Tata Institute of Fundamental Research, Mumbai; Tokyo Metropolitan University, Tokyo and European Synchrotron Radiation Facility, Grenoble for XAS facility. We also acknowledge the XPS facility of IIT, Mandi. We acknowledge the use of ChatGPT (OpenAI) for refining the English language and grammar in the preparation of this manuscript.

References

1 W. Gao, S. Liang, R. Wang, Q. Jiang, Y. Zhang, Q. Zheng, B. Xie, C. T. Toe, X. Zhu, J. Wang, L. Liang Huang, Y. Gao, Z. Wang, C. Jo, Q. Wang, L. Wang, Y. Liu, B. Louis, J. Scott, A. C. Roger, R. Amal, H. Heh and S. E. Park, Industrial Carbon Dioxide Capture and Utilization: State

of the Art and Future Challenges, *Chem. Soc. Rev.*, 2020, **49**, 8584–8686.

2 M. Ghoussoub, M. Xia, P. N. Duchesne, D. Segal and G. A. Ozin, Principles of Photothermal Gas-Phase Heterogeneous CO_2 Catalysis, *Energy Environ. Sci.*, 2019, **12**, 1122.

3 S. Solomon, G. K. Plattner, R. Knutti and P. Friedlingstein, Irreversible Climate Change Due to Carbon Dioxide Emissions, *Proc. Natl. Acad. Sci. U. S. A.*, 2009, **106**, 1704–1709.

4 G. Yin, M. Nishikawa, Y. Nosaka, N. Srinivasan, D. Atarashi, E. Sakai and M. Miyauchi, Photocatalytic Carbon Dioxide Reduction by Copper Oxide Nanocluster-Grafted Niobate Nanosheets, *ACS Nano*, 2015, **9**, 2111–2119.

5 Y. Li, B. Li, D. Zhang, L. Cheng and Q. Xiang, Crystalline Carbon Nitride Supported Copper Single Atoms for Photocatalytic CO_2 Reduction with Nearly 100% CO Selectivity, *ACS Nano*, 2020, **14**, 10552–10561.

6 M. Cai, Z. Wu, Z. Li, L. Wang, W. Sun, A. A. Tountas, C. Li, S. Wang, K. Feng, A. B. Xu, S. Tang, A. Tavasoli, M. Peng, W. Liu, A. S. Helmey, L. He, G. A. Ozin and X. Zhang, Greenhouse-Inspired Supra-Photothermal CO_2 Catalysis, *Nat. Energy*, 2021, **6**, 807–814.

7 X. Zhang, X. Li, D. Zhang, N. Q. Su, W. Yamg, H. O. Everitt and J. Liu, Product Selectivity in Plasmonic Photocatalysis for Carbon Dioxide Hydrogenation, *Nat. Commun.*, 2017, **8**, 14542.

8 D. Mittal, M. Ahlawat and V. G. Rao, Recent progress and challenges in plasmon-mediated reduction of CO_2 to chemicals and fuels, *Adv. Mater. Interfaces*, 2022, 2102383.

9 S. Singh, R. Verma, N. Kaul, J. Sa, A. Punjal, S. Prabhu and V. Polshettiwar, Surface Plasmon-Enhanced Photo-Driven CO_2 Hydrogenation by Hydroxy Terminated Nickel Nitride Nanosheets, *Nat. Commun.*, 2023, **14**, 2551.

10 R. Verma, R. Belgamwar and V. Polshettiwar, Plasmonic Photocatalysis for CO_2 Conversion to Chemicals and Fuels, *ACS Mater. Lett.*, 2021, **3**, 574–598.

11 S. Yu and P. K. Jain, Plasmonic Photosynthesis of C1–C3 Hydrocarbons from Carbon Dioxide Assisted by an Ionic Liquid, *Nat. Commun.*, 2019, **10**, 2022.

12 X. Chen and S. S. Mao, Titanium Dioxide Nanomaterials: Synthesis, Properties, Modifications, and Applications, *Chem. Rev.*, 2007, **107**, 2891–2959.

13 A. Kubacka, M. Fernandez-Garcia and G. Colon, Advanced Nanoarchitectures for Solar Photocatalytic Applications, *Chem. Rev.*, 2012, **112**, 1555–1614.

14 S. N. Habisreutinger, L. Schmidt-Mende and J. K. Stolarczyk, Photocatalytic Reduction of CO_2 on TiO_2 and Other Semiconductors, *Angew. Chem., Int. Ed.*, 2013, **52**, 7372–7408.

15 X. Liu, G. Zhu, X. Wang, X. Yuan, T. Lin and F. Huang, Progress in Black Titania: A New Material for Advanced Photocatalysis, *Adv. Energy Mater.*, 2016, **6**, 1600452.

16 K. Takanabe, Photocatalytic Water Splitting: Quantitative Approaches toward Photocatalyst by Design, *ACS Catal.*, 2017, **7**, 8006–8022.

17 M. Shahrezaei, S. M. H. Hejazi, H. Kmentova, V. Sedajova, R. Zboril, A. Naldoni and S. Kment, Ultrasound-Driven Defect Engineering in TiO_{2-x} Nanotubes-Toward Highly Efficient Platinum Single Atom-Enhanced Photocatalytic Water Splitting, *ACS Appl. Mater. Interfaces*, 2023, **15**(31), 37976–37985.

18 X. Feng, J. D. Sloppy, T. J. LaTempa, M. Paulose, S. Komarneni, N. Bao and C. A. Grimes, Synthesis and deposition of ultrafine Pt nanoparticles within high aspect ratio TiO_2 nanotube arrays: application to the photocatalytic reduction of carbon dioxide, *J. Mater. Chem.*, 2011, **21**, 13429–13433.

19 W. N. Wang, W. J. An, B. Ramalingam, S. Mukherjee, D. M. Niedzwiedzki, S. Gangopadhyay and P. Biswas, Size and Structure Matter: Enhanced CO_2 Photoreduction Efficiency by Size-Resolved Ultrafine Pt Nanoparticles on TiO_2 Single Crystals, *J. Am. Chem. Soc.*, 2012, **134**, 11276–11281.

20 S. I. In, D. D. I. I. Vaughn and R. E. Schaak, Hybrid CuO-$TiO_{2-x}N_x$ Hollow Nanocubes for Photocatalytic Conversion of CO_2 into Methane under Solar Irradiation, *Angew. Chem., Int. Ed.*, 2012, **51**, 3915–3918.

21 J. Liu, Y. Xie, Y. Wang, K. Yang, S. Su, Y. Ling and P. Chen, Synergistic coupling of interface ohmic contact and LSPR effects over Au/$Bi_{24}O_{31}Br_{10}$ nanosheets for visible-light-driven photocatalytic CO_2 reduction to CO, *Chem. Sci.*, 2023, **14**, 13518–13529.

22 O. Henrotte, Š. Kment and A. Naldoni, Interfacial States in Au/Reduced TiO_2 Plasmonic Photocatalysts Quench Hot-Carrier Photoactivity, *J. Phys. Chem. C*, 2023, **127**(32), 15861–15870.

23 P. D. Dongare, Y. Zhao, D. Renard, J. Yang, O. Neumann, J. Metz, L. Yuan, A. Alabastri, P. Nordlander and N. J. Halas, A 3D Plasmonic Antenna-Reactor for Nanoscale Thermal Hotspots and Gradients, *ACS Nano*, 2021, **15**(5), 8761–8769.

24 C. H. P. Camargo and E. Cortés, *Plasmonic Catalysis: From Fundamentals to Applications*, Wiley-VCH, Weinheim, 2021, ISBN: 978-3-527-34750-6.

25 M. Herran, S. Juergensen, M. Kessens, D. Hoeing, A. Köppen, Sousa, A. Castillo, W. J. Parak, H. Lange, S. Reich and F. Schulz, Cortés, E Plasmonic Bimetallic Two-Dimensional Supercrystals for H_2 Generation, *Nat. Catal.*, 2023, **6**, 1205–1214.

26 E. Cortés, L. V. Besteiro, A. Alabastri, A. Baldi, G. Tagliabue, A. Demetriadou and P. Narang, Challenges in plasmonic catalysis, *ACS Nano*, 2020, **14**, 16202–16219.

27 S. Linic, S. Chavez and R. Elias, Flow and Extraction of Energy and Charge Carriers in Hybrid Plasmonic Nanostructures, *Nat. Mater.*, 2021, **20**, 916–924.

28 U. Aslam, V. G. Rao, S. Chavez and S. Linic, Catalytic Conversion of Solar to Chemical Energy on Plasmonic Metal Nanostructures, *Nat. Catal.*, 2018, **1**, 656–665.

29 Z. Geng, Y. Yu, A. J. Offen and J. Liu, Achieving Maximum Overall Light Enhancement in Plasmonic Catalysis by Combining Thermal and Non-thermal Effects, *Nat. Catal.*, 2023, **6**, 1241–1247.

30 O. Henrotte, E. Y. Santiago, A. Movsesyan, L. Mascaretti, M. Afshar, A. Minguzzi, A. Vertova, Z. M. Wang, R. Zbořil, Š. Kment, A. O. Govorov and A. Naldoni, Local Photochemical Nanoscopy of Hot-Carrier-Driven Catalytic Reactions Using Plasmonic Nanosystems, *ACS Nano*, 2023, **17**(12), 11427–11438.
31 S. Swaminathan, J. K. Bera and M. Chandra, Simultaneous Harvesting of Multiple Hot Holes *via* Visible-Light Excitation of Plasmonic Gold Nanospheres for Selective Oxidative Bond Scission of Olefins to Carbonyls, *Angew. Chem., Int. Ed.*, 2023, **62**, e202215933.
32 V. Jain, R. K. Kashyap and P. P. Pillai, Plasmonic Photocatalysis: Activating Chemical Bonds Through Light and Plasmon, *Adv. Optical Mater.*, 2022, 2200463.
33 H. Jiang, L. Wang, H. Kaneko, R. Gu, G. Su, L. Li, J. Zhang, H. Song, F. Zhu, A. Yamaguchi, J. Xu, F. Liu, M. Miyauchi, W. Ding and M. Zhong, Light-Driven CO_2 Methanation over Au-grafted $Ce_{0.95}Ru_{0.05}O_2$ Solid-Solution Catalysts with Activities Approaching the Thermodynamic Limit, *Nat. Catal.*, 2023, **6**, 519–530.
34 A. G. M. da Silva, T. S. Rodrigues, V. G. Correia, T. V. Alves, R. S. Alves, R. A. Ando, F. R. Ornellas, J. Wang, L. H. Andrade and P. H. C. Camargo, Plasmonic Nanorattles as Next-Generation Catalysts for Surface Plasmon Resonance-Mediated Oxidations Promoted by Activated Oxygen, *Angew. Chem., Int. Ed.*, 2016, **55**, 7111–7115.
35 A. Wach, R. Bericat-Vadell, C. Bacellar, C. Cirelli, P. J. M. Johnson, R. G. Castillo, V. R. Silveira, P. Broqvist, J. Kullgren, A. Maximenko, T. Sobol, E. Partyka-Jankowska, P. Nordlander, N. J. Halas, J. Szlachetko and J. Sá, The Dynamics of Plasmon-Induced Hot Carrier Creation in Colloidal Gold, *Nat. Commun.*, 2025, **16**, 2274.
36 S. Griffin, N. P. Montoni, G. Li, P. J. Straney, J. E. Millstone, D. J. Masiello and J. P. Camden, Imaging Energy Transfer in Pt-Decorated Au Nanoprisms *via* Electron Energy-Loss Spectroscopy, *J. Phys. Chem. Lett.*, 2016, **7**, 3825–3832.
37 U. Aslam, S. Chavez and S. Linic, Controlling Energy Flow in Multimetallic Nanostructures For Plasmonic Catalysis, *Nat. Nanotechnol.*, 2017, **12**, 1000–1005.
38 H. Robatjazi, J. L. Bao, M. Zhang, L. Zhou, P. Christopher, E. A. Carter, P. Nordlander and N. J. Halas, Plasmon-driven carbon–fluorine ($C(sp^3)$–F) bond activation with mechanistic insights into hot-carrier-mediated pathways, *Nat. Catal.*, 2020, **3**, 564–573.
39 L. Zhou, J. M. P. Martirez, J. Finzel, C. Zhang, D. F. Swearer, S. Tian, H. Robatjazi, M. Lou, L. Dong, L. Henderson, P. Christopher, E. A. Carter, P. Nordlander and N. J. Halas, Light-Driven Methane Dry Reforming with Single Atomic Site Antenna-Reactor Plasmonic Photocatalysts, *Nat. Energy*, 2020, **5**, 61–70.
40 A. Marimuthu, J. Zhang and S. Linic, Tuning Selectivity in Propylene Epoxidation by Plasmon Mediated Photo-Switching of Cu Oxidation State, *Science*, 2013, **339**, 1590–1593.
41 D. F. Swearer, H. Zhao, L. Zhou, C. Zhang, H. Robatjazi, J. M. P. Martirez, C. M. Krauter, S. Yazdi, M. J. McClaine, E. Ringe, E. A. Carter, P. Nordlander and N. J. Halas, Heterometallic Antenna-Reactor Complexes for Photocatalysis, *Proc. Natl. Acad. Sci. U. S. A.*, 2016, **113**, 8916–8920.
42 C. T. Campbell and C. H. F. Peden, Oxygen Vacancies and Catalysis on Ceria Surfaces, *Science*, 2005, **309**, 713–714.
43 R. J. D. Tilley, Defects in solids, in *Encyclopedia of Inorganic Chemistry*, ed. R. A. Scott, John Wiley & Sons, Ltd, 2008, pp. 1–513.
44 C. Xie, D. Yan, H. Li, S. Du, W. Chen, Y. Wang, Y. Zou, R. Chen and S. Wang, Defect Chemistry in Heterogeneous Catalysis: Recognition, Understanding, and Utilization, *ACS Catal.*, 2020, **10**, 11082–11098.
45 Y. Luo, Y. Wu, A. Braun, C. Huang, X. –Y. Li, C. Menon and P. K. Chu, Defect Engineering to Tailor Metal Vacancies in 2D Conductive Metal–Organic Frameworks: An Example in Electrochemical Sensing, *ACS Nano*, 2022, **16**, 20820–20830.
46 H. Yan, B. Liu, X. Zhou, F. Meng, M. Zhao, Y. Pan, J. Li, Y. Wu, H. Zhao, Y. Liu, X. Chen, L. Li, X. Feng, D. Chen, H. Shan, C. Yang and N. Yan, Enhancing Polyol/Sugar Cascade Oxidation to Formic Acid with Defect Rich MnO_2 Catalysts, *Nat. Commun.*, 2023, **14**, 4509.
47 L. Chen and Q. Xu, Fewer Defects, Better Catalysis?, *Science*, 2020, **367**, 737.
48 J. Yang, Y. Wang, M. J. Lagos, V. Manichev, R. Fullon, X. Song, D. Voiry, S. Chakraborty, W. Zhang, P. E. Batson, L. Feldman, T. Gustafsson and M. Chhowalla, Single Atomic Vacancy Catalysis, *ACS Nano*, 2019, **13**, 9958–9964.
49 R. Verma, C. Singhvi, A. Venkatesh and V. Polshettiwar, Defects tune the acidic strength of amorphous aluminosilicates, *Nat. Commun.*, 2024, **15**, 6899.
50 A. K. Mishra, R. Belgamwar, R. Jana, A. Datta and V. Polshettiwar, Defects in Nanosilica Catalytically Convert CO_2 to Methane Without Any Metal and Ligand, *Proc. Natl. Acad. Sci. U. S. A.*, 2020, **117**, 6383–6390.
51 R. Belgamwar, R. Verma, T. Das, S. Chakraborty, P. Sarawade and V. Polshettiwar, Defects Tune the Strong Metal–Support Interactions in Copper Supported on Defected Titanium Dioxide Catalysts for CO_2 Reduction, *J. Am. Chem. Soc.*, 2023, **145**, 8634–8646.
52 C. Singhvi, G. Sharma, R. Verma, V. K. Paidi, P. Glatzel, P. Paciok, V. B. Patel, O. Mohan and V. Polshettiwar, Tuning the electronic structure and SMSI by integrating trimetallic sites with defective ceria for the CO_2 reduction reaction, *Proc. Natl. Acad. Sci. U.S.A.*, 2025, **122**, e2411406122.
53 V. Polshettiwar, Dendritic Fibrous Nanosilica: Discovery, Synthesis, Formation Mechanism, Catalysis, and CO_2 Capture-Conversion, *Acc. Chem. Res.*, 2022, **55**, 1395–1410.
54 N. Bayal, R. Singh and V. Polshettiwar, Nanostructured Silica-Titania Hybrid using Dendritic Fibrous Nanosilica as a Photocatalyst, *ChemSusChem*, 2017, **10**, 2182–2191.
55 M. Dhiman, A. Maity, A. Das, R. Belgamwar, B. Chalke, Y. Lee, k. Sim, J.-M. Nam and V. Polshettiwar, Plasmonic Colloidosomes of Black Gold for Solar Energy Harvesting and Hotspots Directed Catalysis for CO_2 to Fuel Conversion, *Chem. Sci.*, 2019, **10**, 6594–6603.

56 R. Verma, R. Tyagi, V. K. Voora and V. Polshettiwar, Black Gold-Based "Antenna–Reactor" To Activate Non-Plasmonic Nickel: Photocatalytic Hydrodechlorination and Hydrogenation Reactions, *ACS Catal.*, 2013, **13**, 7395–7406.

57 R. Verma, R. Belgamwar, P. Chatterjee, R. Bericat-Vadell, J. Sa and V. Polshettiwar, Nickel-Laden Dendritic Plasmonic Colloidosomes of Black Gold: Forced Plasmon Mediated Photocatalytic CO_2 Hydrogenation, *ACS Nano*, 2023, **17**, 4526–4538.

58 R. Asahi, T. Morikawa, T. Ohwaki, K. Aoki and Y. Taga, Visible-Light Photocatalysis in Nitrogen-Doped Titanium Oxides, *Science*, 2001, **293**, 269–271.

59 Y. Joly, D. Cabaret, H. Renevier and C. R. Natoli, Electron population Analysis by Full-Potential X-Ray absorption simulations, *Phys. Rev. Lett.*, 1999, **82**(11), 2398–2401.

60 L. Wang, B. Cheng, L. Zhang and J. Yu, *In situ* Irradiated XPS Investigation on S-Scheme $TiO_2@ZnIn_2S_4$ Photocatalyst for Efficient Photocatalytic CO_2 Reduction, *Small*, 2021, **17**, 41.

61 G. Cheng and A. R. Hight Walker, Transmission electron microscopy characterization of colloidal copper nanoparticles and their chemical reactivity, *Anal. Bioanal. Chem.*, 2010, **396**, 1057–1069.

62 H. Liu, S. Li, W. W. Wang, Z. W. Yu, J. W. Zhang, C. Ma and J. C. Jia, Partially Sintered Copper–Ceria as Excellent Catalyst for the High-Temperature Reverse Water Gas Shift Reaction, *Nat. Commun.*, 2022, **13**, 867.

63 X. Yang, S. Wang, H. Sun, X. Wang and J. Lian, Preparation and Photocatalytic Performance of Cu-Doped TiO_2 Nanoparticles, *Trans. Nonferrous Met. Soc. China*, 2015, **25**, 504–509.

64 A. Chen, X. Yu, Y. Zhou, S. Miao, Y. Li, S. Kuld, J. Sehested, J. Liu, T. Aoki, S. Hong, M. F. Camellone, S. Fabris, J. Ning, C. Jin, C. Yang, A. Nefedov, C. Wöll, Y. Wang and W. Shen, Structure of the Catalytically Active Copper–Ceria Interfacial Perimeter, *Nat. Catal.*, 2019, **2**, 334–341.

65 L. Kang, B. Wang, A. T. Güntner, S. Xu, X. Wan, Y. Liu, S. Marlow, Y. Ren, D. Gianolio, C. C. Tang, V. Murzin, H. Asakura, Q. He, S. Guan, J. J. Velasco-Vélez, S. E. Pratsinis, Y. Guo and F. R. Wang, The Electrophilicity of Surface Carbon Species in the Redox Reactions of CuO-CeO_2 Catalysts, *Angew. Chem., Int. Ed.*, 2021, **133**, 14541–14549.

66 W.-W. Wang, P.-P. Du, S.-H. Zou, H.-Y. He, R.-X. Wang, Z. Jin, S. Shi, Y.-Y. Huang, R. Si, Q.-S. Song, C.-J. Jia and C.-H. Yan, Highly Dispersed Copper Oxide Clusters as Active Species in Copper-Ceria Catalyst for Preferential Oxidation of Carbon Monoxide, *ACS Catal.*, 2015, **5**, 2088–2099.

67 P. Liu, H. Wang, X. Li, M. Rui and H. Zeng, Localized Surface Plasmon Resonance of Cu Nanoparticles by Laser Ablation in Liquid Media, *RSC Adv.*, 2015, **5**, 79738–79745.

68 F. Farges, G. E. Brown and J. J. Rehr, TiK-edge XANES studies of Ti coordination and disorder in oxide compounds: comparison between theory and experiment, *Phys. Rev. B:Condens. Matter Mater. Phys.*, 1997, **56**(4), 1809–1819.

69 F. Meng, B. Maurer, F. Peschel, S. Selcuk, M. Hybertsen, X. Qu, C. Vorwerk, C. Draxl, J. Vinson and D. Lu, Multicode benchmark on simulated Ti K-edge x-ray absorption spectra of Ti-O compounds, *Phys. Rev. Mater.*, 2024, **8**(1), 013801.

70 D. J. Mowbray, J. I. Martinez, J. M. G. Lastra, K. S. Thygesen and K. W. Jacobsen, Stability and electronic properties of TiO_2 nanostructures with and without B and N doping, *J. Phys. Chem. C*, 2009, **113**(28), 12301–12308.

71 N. G. Szwacki, P. Fabrykiewicz, I. Sosnowska, F. Fauth, E. Suard and R. Przeniosło, Orthorhombic symmetry and anisotropic properties of rutile TiO_2, *J. Phys. Chem. C*, 2023, **127**(38), 19240–19249.

72 S. C. Ray, D. K. Mishra, A. B. Panda, H. T. Wang, S. Bhattacharya and W. F. Pong, Temperature-Dependent Electronic Structure of TiO_2 Thin Film Deposited by the Radio Frequency Reactive Magnetron Sputtering Technique: X ray Absorption Near-Edge Structure and X ray Photoelectron Spectroscopy, *J. Phys. Chem. C*, 2022, **126**(20), 8947–8952.

73 K.-S. Yang, Y.-R. Lu, Y.-Y. Hsu, C.-J. Lin, C.-M. Tseng, S. Y. H. Liou, K. Kumar, D.-H. Wei, C.-L. Dong and C.-L. Chen, Plasmon-induced visible-light photocatalytic activity of Au nanoparticle-decorated hollow mesoporous TiO_2: a view by X-ray spectroscopy, *J. Phys. Chem. C*, 2018, **122**(12), 6955–6962.

74 C. Yogi, K. Kojima, T. Hashishin, N. Wada, Y. Inada, E. Della Gaspera, M. Bersani, A. Martucci, L. Liu and T.-K. Sham, Size effect of Au nanoparticles on TiO_2 crystalline phase of nanocomposite thin films and their photocatalytic properties, *J. Phys. Chem. C*, 2011, **115**(14), 6554–6560.

75 L. X. Chen, T. Rajh, W. Jäger, J. Nedeljkovic and M. C. Thurnauer, X-ray absorption reveals surface structure of titanium dioxide nanoparticles, *J. Synchrotron Radiat.*, 1999, **6**(3), 445–447.

76 B. Wen, Q. Hao, W. J. Yin, L. Zhang, Z. Wang, T. Wang, C. Zhou, A. Selloni, X. Yang and L. M. Liu, Electronic structure and photoabsorption of Ti^{3+} ions in reduced anatase and rutile TiO_2, *Phys. Chem. Chem. Phys.*, 2018, **20**(26), 17658–17665.

77 B.-H. Lee, S. Park, M. Kim, A. K. Sinha, S. C. Lee, E. Jung, W. J. Chang, K.-S. Lee, J. H. Kim, S.-P. Cho, H. Kim, K. T. Nam and T. Hyeon, Reversible and cooperative photoactivation of single-atom Cu/TiO_2 photocatalysts, *Nat. Mater.*, 2019, **18**(6), 620–626.

78 Z. Pei, H. Zhang, Z.-P. Wu, X. F. Lu, D. Luan and X. W. Lou, Atomically dispersed Ni activates adjacent Ce sites for enhanced electrocatalytic oxygen evolution activity, *Sci. Adv.*, 2023, **9**(26), eadh1320.

79 Q. Shi, X. Zhang, Z. Li, A. Raza and G. Li, Plasmonic Au nanoparticle of a Au/TiO_2–C_3N_4 heterojunction boosts up photooxidation of benzyl alcohol using LED light, *ACS Appl. Mater. Interfaces*, 2023, **15**(25), 30161–30169.

80 Y. Yu, W. Wen, X.-Y. Qian, J.-B. Liu and J.-M. Wu, UV and visible light photocatalytic activity of Au/TiO_2 nanoforests

with Anatase/Rutile phase junctions and controlled Au locations, *Sci. Rep.*, 2017, **7**(1), 41253.

81 L. X. Chen, T. Rajh, Z. Wang and M. C. Thurnauer, XAFS studies of surface structures of TiO_2 nanoparticles and photocatalytic reduction of metal ions, *J. Phys. Chem. C*, 1997, **101**(50), 10688–10697.

82 M. W. Gaultois and A. P. Grosvenor, XANES and XPS investigations of $(TiO_2)_x(SiO_2)_{1-x}$: the contribution of final-state relaxation to shifts in absorption and binding energies, *J. Mater. Chem.*, 2011, **21**(6), 1829–1836.

83 L. Amidani, A. Naldoni, M. Malvestuto, M. Marelli, P. Glatzel, V. D. Santo and F. Boscherini, Probing Long-Lived Plasmonic-Generated charges in TiO_2/Au by High-Resolution X-ray Absorption spectroscopy, *Angew. Chem., Int. Ed.*, 2015, **54**(18), 5413–5416.

84 F. Farges, G. E. Brown, A. Navrotsky, H. Gan and J. J. Rehr, Coordination chemistry of Ti(IV) in silicate glasses and melts: II. Glasses at ambient temperature and pressure, *Geochim. Cosmochim. Acta*, 1996, **60**(16), 3039–3053.

85 R. Q. Zhang and J. S. McEwen, Local Environment Sensitivity of the Cu K-Edge XANES Features in Cu-SSZ-13: Analysis from First-principles, *J. Phys. Chem. Lett.*, 2018, **9**, 3035–3042.

86 C. R. Natoli, Distance Dependence of Continuum and Bound State of Excitonic Resonances in X-ray Absorption Near-edge structure (XANES). In EXAFS and Near Edge Structure III, *Springer Proc. Phys.*, 1984, **2**, 38–42.

87 C. Lamberti and J. A. van Bokhoven, Introduction: Historical Perspective on XAS, in *X-Ray Absorption and X-Ray Emission Spectroscopy*, John Wiley & Sons Ltd, 2016, pp. 1–21.

88 F. de Groot, G. Vanko and P. Glatzel, The 1s X-ray Absorption Pre-edge Structures in Transition Metal oxides, *J. Phys.:Condens. Matter*, 2009, **21**, 104207.

89 K. Bhattacharya, G. P. Mane, V. Rane, A. K. Tripathi and A. K. Tyagi, Selective CO_2 Photoreduction with Cu-Doped TiO_2 Photocatalyst: Delineating the Crucial Role of Cu-Oxidation State and Oxygen Vacancies, *J. Phys. Chem. C*, 2021, **125**(3), 1793–1810.

90 Y.-F. Xu, P. N. Duchesne, L. Wang, A. Tavasoli, A. A. Jelle, M. Xia, J.-F. Liao, D.-B. Kuang and G. A. Ozin, High-Performance Light-Driven Heterogeneous CO_2 Catalysis With Near-Unity Selectivity on Metal Phosphides, *Nat. Commun.*, 2020, **11**, 5149.

91 Z. Wu, C. Li, Z. Li, K. Feng, M. Cai, D. Zhang, S. Wang, M. Chu, C. Zhang, J. Shen, Z. Huang, Y. Xiao, G. A. Ozin, X. Zhang and L. He, Niobium and Titanium Carbides (Mxenes) as Superior Photothermal Supports for CO_2 Photocatalysis, *ACS Nano*, 2021, **15**, 5696–5705.

92 L. Wang, Y. Dong, T. Yan, Z. Hu, F. M. Ali, D. M. Meira, P. M. Duchesne, J. Y. Y. Loh, C. Qiu, E. E. Storey, H. Xu, W. Sun, M. Ghoussoub, N. P. Kherani, A. S. Helmi and G. A. Ozin, Black Indium Oxide a Photothermal CO_2 Hydrogenation Catalyst, *Nat. Commun.*, 2020, **11**, 2432.

93 P. M. Molina, N. Meulendijks, M. Xu, M. A. Verheijen, T. den Hartog, P. Buskens and F. Sastre, Low Temperature Sunlight-Powered Reduction of CO_2 to CO Using a Plasmonic Au/TiO_2 Nanocatalyst, *ChemCatChem*, 2021, **13**, 4507–4513.

94 A. A. Upadhye, R. Insoo, X. Zenga, H. J. Kim, I. Tejedor, M. A. Anderson, J. A. Dumesic and G. W. Hub, Plasmon-Enhanced Reverse Water Gas Shift Reaction over Oxide Supported Au Catalysts, *Catal. Sci. Technol.*, 2015, **5**, 2590–2601.

95 L. Wan, Q. Zhou, X. Wang, T. E. Wood, L. Wang, P. N. Duchesne, J. Guo, X. Yan, M. Xia, Y. F. Li, F. M. Ali, U. Ulmer, J. Jia, T. Li, W. Sun and G. A. Ozin, Cu_2O Nanocubes With Mixed Oxidation-State Facets for (Photo) Catalytic Hydrogenation of Carbon Dioxide, *Nat. Catal.*, 2019, **2**, 889–898.

96 H. Zhang, T. Wang, J. Wang, H. Liu, T. D. Dao, M. Li, G. Liu, X. Meng, K. Chang, L. Shi, T. Nagao and J. Ye, Surface-Plasmon-Enhanced Photodriven CO_2 Reduction Catalyzed by Metal-Organic-Framework-Derived Iron Nanoparticles Encapsulated by Ultrathin Carbon Layers, *Adv. Mater.*, 2016, **28**, 3703–3710.

97 Z. Jia, S. Ning, Y. Tong, X. Chen, H. Hu, L. Liu, J. Ye and D. Wang, Selective photothermal reduction of CO_2 to CO over Ni-nanoparticle/N-doped CeO_2 Nanocomposite Catalysts, *ACS Appl. Nano Mater.*, 2021, **4**, 10485–10494.

98 J. Zhao, Q. Yang, R. Shi, G. I. N. Waterhouse, X. Zhang, L. Z. Wu, C. H. Tung and T. Zhang, FeO–CeO_2 Nanocomposites: An Efficient and Highly Selective Catalyst System for Photothermal CO_2 Reduction to CO, *NPG Asia Mater.*, 2020, **12**, 5.

99 G. Fu, M. Jiang, J. Liu, K. Zhang, Y. Hu, Y. Xiong, A. Tao, Z. Tie and Z. Jin, Rh/Al Nanoantenna Photothermal Catalyst for Wide-Spectrum Solar-Driven CO_2 Methanation With Nearly 100% Selectivity, *Nano Lett.*, 2021, **21**, 8824–8830.

100 B. Tahir, M. Tahir and N. A. S. Amin, Photocatalytic CO_2 Conversion Over Au/TiO_2 Nanostructures for Dynamic Production of Clean Fuels in a Monolith Photoreactor, *Clean Technol. Environ. Policy*, 2016, **18**, 2147–2160.

101 M. Tahir, B. Tahir and N. A. S. Amin, Synergistic Effect in Plasmonic Au/Ag Alloy NPs Co-coated TiO_2 NWs Toward Visible-Light Enhanced CO_2 Photoreduction to Fuels, *Appl. Catal., B*, 2017, **204**, 548–560.

102 J. Jia, H. Wang, Z. Lu, P. G. O'Brien, M. Ghoussoub, P. Duchesne, Z. Zheng, P. Li, Q. Qiao, L. Wang, A. Gu, A. A. Jelle, Y. Dong, Q. Wang, K. K. Ghuman, T. Wood, C. Qian, Y. Shao, C. Qiu, M. Ye, Y. Zhu, Z.-H. Lu, P. Zhang, A. S. Helmy, C. V. Singh, N. P. Kherani, D. D. Perovic and G. A. Ozin, Photothermal Catalyst Engineering: Hydrogenation of Gaseous CO_2 with High Activity and Tailored Selectivity, *Adv. Sci.*, 2017, **4**, 1700252.

103 M. Tahir, B. Tahir, N. A. S. Amin and Z. Y. Zakaria, Photo-induced Reduction of CO_2 to CO with Hydrogen over Plasmonic Ag-NPs/TiO_2 NWs Core/shell Hetero-junction under UV and Visible light, *J. CO2 Util.*, 2017, **18**, 250–260.

104 H. Robatjazi, H. Zhao, D. F. Swearer, N. J. Hogan, L. Zhou, A. Alabastri, M. J. McClain, P. Nordlander and N. J. Halas, Plasmon-induced Selective Carbon Dioxide Conversion on

Earth-Abundant Aluminum-Cuprous Oxide Antenna-Reactor Nanoparticles, *Nat. Commun.*, 2017, **8**, 27.

105 F. Sastre, A. V. Puga, L. Liu, A. Corma and H. García, Complete Photocatalytic Reduction of CO_2 to Methane by H_2 under Solar Light Irradiation, *J. Am. Chem. Soc.*, 2014, **136**, 6798–6801.

106 J. Y. Y. Loh, A. Mohan, A. G. Flood, G. A. Ozin and N. P. Kherani, Waveguide Photoreactor Enhances Solar Fuels Photon Utilization Towards Maximal Optoelectronic – Photocatalytic Synergy, *Nat. Commun.*, 2021, **12**, 402.

107 N. G. J, I. García-García, T. Perfrement, E. C. Lovell, T. W. Schmidt, J. Scott and R. Amal, Plasmonic Effects on CO_2 Reduction over Bimetallic Ni-Au Catalysts, *Chem. Eng. Sci.*, 2019, **194**, 94–104.

108 M. Li, P. Li, K. Chang, T. Wang, L. Liu, Q. Kang, S. Ouyang and J. Ye, Highly Efficient and Stable Photocatalytic Reduction of CO_2 to CH_4 over Ru Loaded $NaTaO_3$, *Chem. Commun.*, 2015, **51**, 7645–7648.

109 W. Sun, C. Qian, L. He, K. K. Ghuman, A. P. Y. Wong, J. Jia, A. A. Jelle, P. G. O'Brien, L. M. Reyes, T. E. Wood, A. S. Helmy, C. A. Mims, C. V. Chandra Veer Singh and G. A. Ozin, Heterogeneous Reduction of Carbon Dioxide by Hydride-Terminated Silicon Nanocrystals, *Nat. Commun.*, 2016, **7**, 12553.

110 Y. F. Li, W. Lu, K. Chen, P. Duchesne, F. M. Ali, M. Xia, T. E. Wood, U. Ulmer and G. A. Ozin, Cu Atoms on Nanowire Pd/$HyWO_{3-x}$ Bronzes Enhance the Solar Reverse Water Gas Shift Reaction, *J. Am. Chem. Soc.*, 2019, **141**, 14991–14996.

111 C. Qian, W. Sun, D. L. H. Hung, C. Qiu, M. Makaremi, S. G. H. Kumar, L. Wan, M. Ghoussoub, T. E. Wood, M. Xia, A. A. Tountas, Y. F. Li, L. Wang, Y. Dong, I. Gourevich, C. V. Singh and G. A. Ozin, Catalytic CO_2 Reduction by Palladium-Decorated Silicon–Hydride Nanosheets, *Nat. Catal.*, 2019, **2**, 46–54.

112 A. A. Jelle, K. K. Ghuman, P. G. O'Brien, M. Hmadeh, A. Sandhel, D. D. Perovic, C. V. Singh, C. A. Mims and G. A. Ozin, Highly Efficient Ambient Temperature CO_2 Photomethanation Catalyzed by Nanostructured RuO_2 on Silicon Photonic Crystal Support, *Adv. Energy Mater.*, 2018, **8**, 1702277.

113 D. Mateo, N. Morlanes, P. Maity, G. Shterk, O. F. Mohammed and J. Jorge Gascon, Efficient Visible-Light Driven Photothermal Conversion of CO_2 to Methane by Nickel Nanoparticles Supported on Barium Titanate, *Adv. Funct. Mater.*, 2021, **31**, 2008244.

114 P. G. O'Brien, A. Sandhel, T. E. Wood, A. A. Jelle, L. B. Hoch, D. D. Perovic, C. A. Mims and G. A. Ozin, Photomethanation of Gaseous CO_2 over Ru/silicon Nanowire Catalysts with Visible and Near-infrared Photons, *Adv. Sci.*, 2014, **1**, 1400001.

115 D. Mateo, J. Albero and H. García, Graphene Supported NiO/Ni Nanoparticles as Efficient Photocatalyst for Gas Phase CO_2 Reduction with Hydrogen, *Appl. Catal., B*, 2018, **224**, 563–571.

116 V. Golovanova, M. C. Spadaro, J. Arbiol, V. Golovanov, T. T. Rantala, T. Andreu and J. R. Morante, Effects of Solar Irradiation on Thermally Driven CO_2 Methanation using Ni/CeO_2-based Catalyst, *Appl. Catal., B*, 2021, **291**, 120038.

117 S. Wang, M. Cabrero-Antonino, S. Navalón, C.-C. Cao, A. Tissot, I. Dovgaliuk, J. Marrot, C. Martineau-Corcos, L. Yu, H. Wang, W. Shepard, H. Garcia and C. Serre, A Robust Titanium Isophthalate Metal-Organic Framework for Visible-Light Photocatalytic CO_2 Methanation, *Chem*, 2020, **6**, 3409–3427.

118 D. Mateo, J. Albero and H. Garcia, Titanium-Perovskite-supported RuO_2 Nanoparticles for Photocatalytic CO_2 Methanation, *Joule*, 2019, **3**, 1949–1962.

119 Y. Xiong, H. Chen, Y. Hu, S. Yang, X. Xue, L. He, X. Liu, J. Ma and Z. Jin, Photodriven Catalytic Hydrogenation of CO_2 to CH_4 with Nearly 100% Selectivity over Ag25 clusters, *Nano Lett.*, 2021, **21**, 8693–8700.

120 C. J. Bueno-Alejo, A. Arca-Ramos, J. L. Hueso and J. Santamaria, LED-driven Continuous Flow Carbon Dioxide Hydrogenation on a Nickel-based Catalyst, *Catal. Today*, 2020, **355**, 678–684.

121 X. Li, O. H. Everitt and J. Liu, Confirming Nonthermal Plasmonic Effects Enhance CO_2 Methanation on Rh/TiO_2 Catalysts, *Nano Res.*, 2019, **12**, 1906–1911.

122 P. Christopher, H. Xin, A. Marimuthu and S. Linic, Singular Characteristics and Unique Chemical Bond Activation Mechanisms of Photocatalytic Reactions on Plasmonic Nanostructures, *Nat. Mater.*, 2012, **11**, 1044–1050.

123 C. Xu, W. Huang, Z. Li, B. Deng, Y. Zhang, M. Ni and K. Cen, Photothermal Coupling Factor Achieving CO_2 Reduction Based on Palladium-Nanoparticle-Loaded TiO_2, *ACS Catal.*, 2018, **8**, 6582–6593.

124 S. Chen, Y. Xiao, Y. Wang, Z. Hu, H. Zhao and W. Xie, A Facile Approach to Prepare Black TiO_2 with Oxygen Vacancy for Enhancing Photocatalytic Activity, *Nanomaterials*, 2018, **8**, 245.

125 K. S. Yang, Y. R. Lu, Y. Y. Hsu, C. J. Lin, C. M. Tseng, S. Y. H. Liou, K. Kumar, D. H. Wei, C. L. Dong and C. L. Cheng, Plasmon-Induced Visible-Light Photocatalytic Activity of Au Nanoparticle-Decorated Hollow Mesoporous TiO_2: A View by X-ray Spectroscopy, *J. Phys. Chem. C*, 2018, **122**, 6955–6962.

126 G. S. Henderson, F. M. F. de Groot and B. J. A. Moulton, X-ray Absorption Near-edge Structure (XANES) Spectroscopy, *Rev. Mineral. Geochem.*, 2014, **78**, 75–138.

127 H. Tang, C. J. Chen, Z. Huang, J. Bright, G. Meng, R. S. Liu and N. Wu, Plasmonic Hot Electrons for Sensing, Photodetection, and Solar Energy Applications: A Perspective, *J. Chem. Phys.*, 2020, **152**, 220901.

128 C. Lee, Y. Park and J. Y. Park, Hot Electrons Generated by Intraband and Interband Transition Detected Using a Plasmonic Cu/TiO_2 Nanodiode, *RSC Adv.*, 2019, **9**, 18371–18376.

129 W. T. Figueiredo, G. B. Della Mea, M. Segala, D. L. Baptista, C. Escudero, V. Pérez-Dieste and F. Bernardi, Understanding the Strong Metal–Support Interaction (SMSI) Effect in Cu_xNi_{1-x}/CeO_2 $(0 < x < 1)$ Nanoparticles

for Enhanced Catalysis, *ACS Appl. Nano Mater.*, 2019, **2**, 2559–2573.

130 X. Du, Y. Huang, X. Pan, B. Han, Y. Su, Q. Jiang, M. Li, H. Tang, G. Li and B. Qiao, Size-dependent strong metal-support interaction in TiO_2 supported Au nanocatalysts, *Nat. Commun.*, 2020, **11**, 5811.

131 X. Su, X. Yang, B. Zhao and Y. Huang, Designing of Highly Selective and High-Temperature Endurable RWGS Heterogeneous Catalysts: Recent Advances and the Future Directions, *J. Energy Chem.*, 2017, **26**, 854–867.

132 F. C. Meunier, D. A. Reid, S. Goguet, C. Shekhtman; Hardacre, R. Burch, W. Deng and M. Flytzani-Stephanopoulos, Quantitative Analysis of the Reactivity of Formate Species Seen by DRIFTS over an $Au/Ce(La)O_2$ Water–gas Shift Catalyst: First Unambiguous Evidence of the Minority Role of Formates as Reaction Intermediates, *J. Catal.*, 2007, **242**, 277–287.

133 Y. Wang, S. Kattel, W. Gao, *et al.*, Exploring the Ternary Interactions in $Cu–ZnO–ZrO_2$ Catalysts for Efficient CO_2 Hydrogenation to Methanol, *Nat. Commun.*, 2019, **10**, 1166.

134 J. Yu, X. Sun, X. Tong, J. Zhang, J. Li, S. Li, Y. Liu, N. Tsubaki, T. Abe and J. Sun, Ultra-high Thermal Stability of Sputtering Reconstructed Cu-based Catalysts, *Nat. Commun.*, 2021, **12**, 7209.

135 J. Schumann, J. Kröhnert, E. Frei, R. Schlögel and A. Trunschke, IR-Spectroscopic Study on the Interface of Cu-based Methanol Synthesis Catalysts: Evidence for the Formation of a ZnO Overlayer, *Top. Catal.*, 2017, **60**, 1735–1743.

136 E. Garand, T. Wende, D. J. Goebbert, R. Bergmann, G. Meijer, D. M. Neumark and K. R. Asmis, Infrared Spectroscopy of Hydrated Bicarbonate Anion Clusters: $HCO_3^-(H_2O)_{1-10}$, *J. Am. Chem. Soc.*, 2010, **132**(2), 849–856.

137 R. Verma, G. Sharma and V. Polshettiwar, The Paradox of Thermal *vs.* Non-Thermal Effects in Plasmonic Photocatalysis, *Nat. Commun.*, 2024, **15**, 7974.

138 G. Sharma, R. Verma, S. Masuda, K. M. Badawy, N. Singh, T. Tsukuda and V. Polshettiwar, Pt-doped Ru nanoparticles loaded on 'black gold' plasmonic nanoreactors as air stable reduction catalysts, *Nat. Commun.*, 2024, **15**, 713.

139 Y. Dubi and Y. Sivan, "Hot" electrons in metallic nanostructures—non-thermal carriers or heating?, *Light:Sci. Appl.*, 2019, **8**, 89.

140 Y. Dubi, I. W. Un and Y. Sivan, Distinguishing thermal from nonthermal ("hot") carriers in illuminated molecular junctions, *Nano Lett.*, 2022, **22**, 2127–2133.

141 R. Kamarudheen, G. W. Catellanos, L. J. P. Kamp, H. J. H. Clercx and A. Baldi, Quantifying photothermal and hot charge carrier effects in plasmon-driven nanoparticle syntheses, *ACS Nano*, 2018, **12**, 8447–8455.